Applied Energy 317 (2022) 119143

Contents lists available at ScienceDirect

Applied Energy

journal homepage: www.elsevier.com/locate/apenergy

Benchmarking solid oxide electrolysis cell-stacks for industrial Power-to-Methane systems via hierarchical multi-scale modelling

Lukas Wehrle [a], Daniel Schmider [a,b], Julian Dailly [b], Aayan Banerjee [c], Olaf Deutschmann [a,*]

[a] Institute for Chemical Technology and Polymer Chemistry, Karlsruhe Institute of Technology, Kaiserstraße 12, 76131 Karlsruhe, Germany
[b] European Institute for Energy Research (EIFER), Emmy-Noether-Straße 11, 76131 Karlsruhe, Germany
[c] Catalytic Processes and Materials, Faculty of Science and Technology, University of Twente, Drienerlolaan 5, 7500 AE Enschede, the Netherlands

HIGHLIGHTS

- Comprehensive validation and parametrization of 2D single cell and 3D stack models.
- Specific threshold conversions of 80% (ESC) and 75% (CSC) which maximize efficiency.
- Performance boost for CSC and losses for ESC design under pressurized conditions.
- Feasible stack operation only at thermoneutral to moderately exothermic conditions.
- CSC-stack reaches doubled H_2-output at 700 °C compared to ESC-stack at 850 °C.

GRAPHICAL ABSTRACT

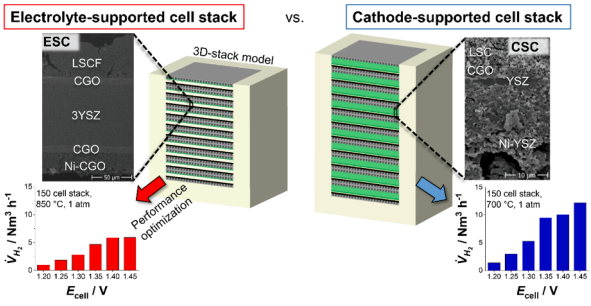

ARTICLE INFO

Keywords:
Solid oxide electrolysis cell (SOEC)
Power-to-Methane
Multi-scale modelling
3D stack model
Optimization

ABSTRACT

Power-to-Gas (PtG) is prognosticated to realize large capacity increases and create substantial revenues within the next decade. Due to their inherently high efficiencies, solid oxide electrolysis cells (SOECs) have the potential to become one of the core technologies in PtG applications. While thermal integration of the high-temperature SOEC module with downstream exothermic methanation is a very potent concept, the performance of SOECs needs to be boosted to amplify the technologies impact for future large-scale plants. Here, we use a combined experimental and modelling approach to benchmark commercial electrolyte- (ESC) and cathode-supported cell (CSC) designs on industrial-scale planar SOEC stack performance. In a first step, comprehensive electrochemical and microstructural analyses are carried out to parametrize, calibrate and validate a detailed multi-physics 2D cell model, which is then used to study the cells' behaviour in detail. The analysis reveals that there exists a cell-specific threshold steam conversion of ~80% for the ESC and ~75% for the CSC design, which represents a maximum of the total (heat plus electrical) electrolysis efficiency. Moreover, while the ESC-design suffers from performance reductions under pressurized conditions, considerable performance increases of ~9% at 20 atm (700 °C, 1.35 V) compared to atmospheric pressure are predicted for the CSC design, showcasing a unique advantage of the CSC cell for process integration with the catalytic methanation. Subsequently, based on a 3D stack model, a scale-up to the industrial stack size is conducted. To comparatively assess stack performances under application-oriented conditions, optimization studies are carried out for 150-cell stack units based on the two cell designs individually. When optimally selecting the stack operation points, the model predicts the CSC-based stack to reach a high capacity up to 36.6 kW (~10.6 Nm^3 H_2 h^{-1}) at 1.35 V and 700 °C, whilst ensuring

* Corresponding author.
E-mail address: deutschmann@kit.edu (O. Deutschmann).

https://doi.org/10.1016/j.apenergy.2022.119143
Received 29 December 2021; Received in revised form 28 March 2022; Accepted 14 April 2022
Available online 26 April 2022

reasonably low temperature gradients (<10 K cm^{-1}) and sweep gas cooling requirements (<30 sccm cm^{-2}). Thus, CSC-design stacks incorporating such a highly active cell design can be expected to further boost the competitiveness of high-temperature electrolysis in PtG plant concepts.

Nomenclature

Latin

A	area [m^2] or pre-exponential factor
C_p	specific heat capacity at constant pressure [J kg^{-1} K^{-1}]
d	diameter [m]
E	electric potential difference [V] or activation energy [J mol^{-1}]
i	current density [A m^{-2}]
$i_{0,r}$	exchange current density of rth charge-transfer reaction [A m^{-2}]
L	length [m]
LHV	lower heating value [J kg^{-1}]
$\dot{m}$	mass flux [kg s^{-1}]
n	pressure exponent or absolute number
$\dot{n}$	molar flux [mol s^{-1}]
p	pressure [atm]
P	power [W]
$\dot{Q}$	heat flux [W m^{-2}]
R	universal gas constant [J mol^{-1} K^{-1}] or specific resistance [Ω cm^2]
SC	steam conversion
t	thickness [m]
T	temperature [K]
$\dot{V}$	volume flux [m^3 s^{-1}]
W	specific energy demand [J m^{-3}]
w	width [m]
X	molar fraction
x	spatial coordinate [m]
y	spatial coordinate [m]
z	spatial coordinate [m]

Greek

β	charge transfer coefficient
δ	extra oxygen vacancies in CGO
ε	porosity
ε_{rad}	thermal radiation emissivity
η	efficiency
λ	thermal conductivity [W m^{-1} K^{-1}]
λ^{V}_{TPB}	specific active triple-phase boundary length [m^{-2}]
ν_f	solid phase volume fraction
σ	charge conductivity [S m^{-1}]
τ_{fac}	tortuosity factor
ψ_{air}	excess air ratio

Subscripts

∞	reference conditions
a	anodic
air	air
an	anode
avg	average
bl	barrier layer
BoP	Balance of plant
c	cathodic
cd	cathode
cell	cell
ch	channel
contact	contact
dl	diffusion layer
ede	electrode
el	electronic phase
elec	electrical
elyt	electrolyte
F	Faradaic
fl	functional layer
g, gas	gas phase
i	due to current
ic	interconnect
in	inlet
io	ionic phase
k	kth species
LHV	lower heating value
m	phase index
max	maximum
ohm	ohmic
out	outlet
p	particle
pol	polarization
pore	pore
q	stack component index
r	reaction index
rib	interconnect rib
s	solid phase or surface
stack	stack
sys	system

Superscripts

eff	effective
V	volumetric

1. Introduction

The ambitious energy policies emerging from climate protection commitments request a significant reduction of green-house gas emissions in all of the energy-consuming sectors and a renunciation of fossil energy sources. However, the envisioned transition to a flexible and sector-coupling energy network can only be accomplished via a commercial roll-out of green energy production processes and an appropriate energy storage concept at a massive scale [1]. By converting the intermittent electrical power supply from renewable energy sources (RES) to persistent chemical energy, Power-to-Gas (PtG) presents an attractive chemical storage concept enabling the coupling of RES with the gas grid, and thus is the subject of extensive research efforts [2–4], as well as exponential increases of installed capacities [5]. One of the core components in such a concept is the electrolyzer splitting water into H_2 and O_2 via the supply of electrical power. Solid oxide electrolysis cells (SOEC) operate at elevated temperatures, which accompanies several challenges, such as thermo-mechanical stability of the cell components, dynamic operation of the SOEC unit and its system integration. Nevertheless, high temperature (HT) operation gives rise to thermodynamic and kinetic advantages over the more established low-temperature (LT) electrolysis technologies, i.e. alkaline electrolysis (AE) and polymer electrolyte membrane (PEM) cells, which enables the production of H_2

at very high electrical efficiencies [1,6–8].

Still, to reach high net system efficiencies with HT-cells, industrial waste heat sources must be available. This makes SOEC-based PtG concepts involving a downstream exothermic reaction process potent in terms of exploiting thermal integration synergies [9–11]. Storing the renewable energy supply in the form of CH_4 has the essential benefits of a versatile and high density energy carrier, which is easily transported and distributed by injecting synthetic natural gas (SNG) into the already existing gas grid infrastructure [12]. Moreover, CH_4 is frequently used for stationary district- and domestic level heating or co-generation in combined heat and power (CHP) plants, and could replace conventional gasoline or diesel fuels in the mobility sector in the near-future [13].

While SOECs can also be operated in H_2O/CO_2 co-electrolysis mode to directly produce syngas at different H_2/CO-ratios [14,15], and pressurized co-electrolysis operation promoting internal methanation within the SOEC-unit has also been studied [16], this work specifically focuses on SOEC stacks performing steam electrolysis for integration into a Power-to-Methane (PtM) plant concept. Some of the studies concepts and outcomes are, however, also applicable for integration of an SOEC-unit into other PtG concepts up to a certain extent, cf. Section 3.3.2. In an integrated PtM system, both the SOEC electrolyzer module, which is electrically connected to a RES, and a CO_2 source are coupled to a catalytic methanation unit. The liquid cooling system of the methanation unit essentially represents the steam generation unit for the SOEC stack, since the reactors operate exothermically based on the Sabatier reaction [9,10]. The integrated SOEC-PtM system's large technological potential is evident from proposed system efficiencies (with respect to the higher heating value (HHV) of the target product) in the range of $\eta_{elec,HHV} \sim$ 80–86% based on a proof-of-concept experimental study involving a pilot demonstrator [9] and system modelling efforts [17–19] for SOEC units coupled to catalytic methanation. Thereby, substantially higher efficiencies can be reached than for plants using LT-electrolysis [20].

While the principle feasibility and the high efficiency of a SOEC-based PtM-concept has been demonstrated [9], cell- and stack-level performance improvements are highly desired to boost the H_2 production capacity, and to pave the way for achieving market-readiness. With current commercially available SOEC systems being based on an electrolyte-supported cell (ESC) configuration containing a relatively thick central layer typically made of doped zirconia [11], operation temperatures are restricted to $\geq$ 800 °C to reach an appropriate current density due to the cells' relatively high ohmic resistance, i.e., area-specific resistance (ASR). These cells are superior in terms of mechanical and electrochemical long-term stability both at steady conditions, as e.g. demonstrated at a high current density of -0.9 A cm^{-2} over 23,000 h with a voltage degradation of 7.4 mV per 1000 h [21], and under load cycling conditions, e.g. 80,000 on/off cycles with losses of 5 mV per 1000 h [22].

Nevertheless, it was also demonstrated that cathode-supported cells (CSC) designed for operation at a lower temperature range can also achieve robustness for continuous steam electrolysis. By tailoring the Ni-yttria-stabilized zirconia (YSZ) electrode microstructure in a CSC to hinder Ni depletion, low degradation rates of 0.3–0.4% per 1000 h up to a current density of ~-1 A cm^{-2} were proven [23], while more recently, solution infiltration of CGO nanoparticles into the Ni-YSZ electrode was shown to significantly reduce CSC degradation [24], demonstrated for 8750 h of operation at a high current density of -1.25 A cm^{-2} with a voltage degradation of 39 mV per 1000 h. Thus, although SOEC plant sizes are expected to markedly increase in the following years [1], given that the maximum SOEC system capacity is currently (beginning of 2022) 720 kW_{elec} (200 Nm^3 h^{-1} H_2) [25], with single electrolyzer stacks having capacities in the range of ~3–15 kW_{elec} [16], stack-level performance improvements by incorporating such highly active cell designs are essential, aside from the scale-up efforts by increasing the SOEC stack tower or module dimensions, in order to cost-competitively meet the demands of the catalytic methanation unit, e.g. ~108.400 Nm^3 h^{-1} H_2 for a 300 MW (based on CH_4 output) industrial-scale PtM-plant [3].

Aside from the power capacity gains decreasing the SOEC module's installation costs, i.e., capital expenditure (CAPEX), potential benefits of a lowered operation temperature also comprise various aspects, including (i) faster thermal cycling, (ii) lower investment costs for stack, insulation and balance of plant (BoP) materials, (iii) decreased heat losses and (iv) lowered electrical heating costs, since electrical heaters to overheat the steam will be at least temporarily required in a real-world plant despite thermal integration.

From a modelling perspective, there exist several studies which performed PtM-system level process modelling with particular focus on reactor design [17], techno-economics [26,27], conceptual design optimization [18,19,28], and thermal integration [10,19], while lab-scale SOEC steam- or co-electrolysis cell-level modelling was conducted e.g. to study pressurized operation [29,30], outlet gas composition [31], degradation mechanisms [32] and temperature distributions [33]. Moreover, when not limiting the literature scope to electrolysis operation only, there exist 3-D stack models mostly based on computational fluid dynamics (CFD) or homogenization approaches, which were used to investigate spatially-resolved temperature distributions, flow fields or stresses [34–37].

However, to the author's best knowledge, an in-depth multi-scale modelling study including a 3D-stack-level simulation tool to analyse the impact of different cell designs on commercial-scale SOEC performance for industrial PtM applications has not yet been conducted. While there exist review papers [8,38–40] and experimental studies [41–43] comparing membrane electrolyte assembly (MEA) materials, cell configurations and stack designs with respect to SOEC performance, detailed modelling studies targeting a benchmarking of different cell concepts are scarce in the literature, but highly required to predictively project the lab-scale findings to the industrially relevant stack and system scale [15]. Additionally, simplified approaches to predict SOEC stack performance on ~100 cell-level that do not resolve the 3D temperature profile (including the insulation layer) and/or neglect the impact of heat exchange with the surroundings might not be valid under realistic conditions, since the large thermal mass of a large-capacity stack complicates an accurate prediction of the local gas and solid phase temperatures. However, this is of crucial importance to realistically predict the SOEC unit's electrochemical performance due to the strong interaction between the stack's thermal behavior and the process variables, such that e.g. operation conditions that are practically not feasible due to the development of large temperature fluctuations across the stack can be reliably accounted for.

Following this outline, this study aims to comparatively assess and optimize industrial-scale SOEC stack performance under conditions specific to industrial PtM plants based on commercial ESC and CSC designs with a particular focus on the stack's thermal behaviour. To achieve this target, a combined modelling plus experimental approach is followed, comprising of (i) a multi-scale computational framework, (ii) polarization and impedance measurements to characterize the cells' electrochemical performances and (iii) microstructural analyses to accurately parametrize the model. This study is structured in the following way: In a first step, the experimental cell characterizations serve to calibrate and validate the cell model. Afterwards, parametric performance analyses are conducted to study the cell behaviour in detail, as well as to reasonably confine the parameter spaces for the stack simulations. Finally, on the industrially-sized stack level, optimization studies with the full 3D model are conducted for stack units based on the two cell designs individually.

2. Methodology

2.1. Modelling

The SOEC modelling tool is based on a mathematical framework previously published by our group [15,44]. Its continuum-level physico-chemical representation of the coupled transport and electrochemical

phenomena occurring within an SOEC single cell or stack are briefly presented by the following bullet points, while a description of the numerical solution procedure is provided afterwards. Additionally, Table S1 and Table S2 give an overview of all the model equations used throughout the study.

2.1.1. Modelling framework and assumptions

- The modelling framework is based on a macro-homogeneous description of the heterogeneous microstructure of an electrode, i.e. the sintered granular and porous nature is characterized statistically in terms of volume-averaged properties based on coordination number and percolation theory.
- The convective gas transport in axial direction along the cell length is described by a one-dimensional plug-flow model. The plug-flow assumption is justified for (i) the channel-type situation in single cell setups and for (ii) the gas channels formed within the bipolar co-flow interconnect structure in stacks due to the low mean velocities typically encountered, i.e. a laminar and highly viscous flow field is developed very near the channel entrance, and the rapid species diffusion along the channel height in radial direction [45]. Axial diffusion is neglected due the significantly higher convective than axial diffusive velocities of the gas-phase species [45], and isobaric conditions are assumed, since pressure losses due to wall shear-stress within the rectangular channels are negligibly small [46,47].
- The species transport within the porous electrodes perpendicular to the bulk gas flow is one-dimensional along the cell thickness, and represented by the Dusty-Gas model, accounting for coupled molecular and Knudsen diffusion, along with advective Darcy flow driven by a pressure gradient due to non-equimolar reactions, i.e. oxygen evolution reaction in the anode.
- The axisymmetric radial co-flow configuration of the tested circular cells in the custom-made test bench is represented in the single cell model geometry by using a half diameter channel length [46].
- Local electrochemistry is described by a global kinetic Butler-Volmer (BV) approach coupled to the mass and charge balances based on empirical power laws. A distributed charge transport model is solved one-dimensionally along the electrode thickness. Mixed ionic and electronic conduction (MIEC) behaviour of single-phase anodes is modelled by establishing individual ionic and electronic charge balances, which are solved for their reduced electrochemical phase potential. This implies that the charge fluxes across the MIEC bulk are proportional to the respective phase conductivity and to the electrochemical potential gradient, though charge carrier profiles are not explicitly resolved.
- Due to the presence of a dense YSZ electron blocking layer with a minimum of $\sim$4 μm thickness in the cell configurations, an electronic leakage current across the electrolyte is not considered.
- For all simulations, the plug-flow model accounts for the gas phase temperature solution in the channels. As apparent from Table S1, the solid phase temperature solution is 2-D along the axial and radial directions and solved for all solid components individually in case of a single cell, whereas full 3-D heat transport is solved for stack simulations. Still, in the latter case, all the solid (dense or porous) constituents are lumped into a single phase with effective thermal properties, whereby local temperature fluctuations across the solid components of the single repeating units are neglected due to the large thermal mass of the stack [48]. For both cases, the solid phase temperature balance equation is decoupled from the rest of the differential algebraic system of equations (DAE) due to the intrinsically larger time scale of heat transport in solids compared to the physics occurring within a single cell or repeating unit (RU) [15,49].
- Current collection is perfect in single cell setups due to optimal contacting with an Au grid and a Ni mesh. In a stack, the presence of the ferritic interconnectors imposes an electrical contact resistance, while the contact layers and protective coatings facilitating current collection are assumed to be dense and placed as stripes between the ribs and electrodes. The interconnectors themselves are perfect electronic conductors.
- For stack simulations, the cell area underneath the interconnect rib is assumed to be electrochemically inactive, i.e., in-plane species diffusion underneath the ribs is not considered. While this assumption is justified for the ESC design due to the interconnect rib width being significantly larger than the Ni-CGO cathode thickness leading to severe species depletion zones [50], it represents a limitation in case of the CSC design with its thicker Ni-YSZ electrode. The implications of this assumption are briefly discussed in Section 3.3.1 with the help of experimental data.
- The inlet and outlet manifolds providing the stack reactant supply are not part of the model.

2.1.2. Numerical solution procedure

The codes used for all simulations throughout the study are part of the FORTRAN-based software package DETCHEM^{TM} [51]. To solve the coupled conservation laws of mass, momentum, charge, and energy, a finite-volume approach was employed by discretizing the modelling domain into a numerical grid. By approximating the spatial derivatives as finite differences, the coupled partial differential equations are converted to a DAE, which then can be solved semi-implicitly and transiently by employing the time-adaptive solver LIMEX [52]. A damped Newton-iteration solver is used to solve the charge balances, which are non-linear algebraic constraints within the DAE setting [53]. For both the single cell and stack simulations, the 2-D or 3-D heat balance equation of the solid phase was decoupled from the rest of the DAE, forming an outer integration loop [15,49].

For the single cell simulations, a 1D + 1D grid along the axial and radial coordinates was defined. The axial flow direction was discretized into 100 equidistant cells and the radial direction into 65 (ESC) or 80 (CSC) cells with varying heights, depending on the thickness of the MEA components, yielding a total number of 6500 or 8000 grid points. Grid independency was checked by doubling the number of grid points in each dimension. A maximum deviation of $< 3\%$ was found in the model results, which is considered to be reasonable.

For stack simulations, the number of grid points in axial direction was raised to 140, due to the increased length of the single RU compared to the single cell. Since an industrial-scale stack consists of a large number of RUs (i.e., 3600 based on the applied geometry), the solution of each RU would become the bottleneck in terms of computation time. In order to make the solution procedure more computationally efficient, an agglomeration algorithm is used, which groups several RUs into clusters according to the local stack temperature field. After several agglomeration steps, multiple clusters have been formed, and the solution algorithm chooses a representative RU from each of the clusters which are then solved in detail. RUs being part of a local temperature field are assumed to behave equivalently. In our work, RUs having a mean temperature difference of $\Delta T \leq 5$ K are grouped into a cluster, since this value was considered to be a reasonable trade-off between computational speed and accuracy. More details regarding the transient solution method for stacks developed by our group can be found elsewhere [49]. At the edges of the stack modelling domain, an insulation layer was implemented accounting for heat flux continuity and individual material properties.

Utilizing this numerical approach, the single cell simulations yielded a steady-state solution typically within $\sim$5 min, while a stack simulation converged in $<$ 8 h on a 3 GHz 6-core processor. The software tool CaRMeN was used to automate the modelling workflow for the single cell calibration procedure, as well as for the parametric single cell analyses [54].

2.1.3. Optimization study

The problem definition for the stack-scale optimization study performed in Section 3.3.2 by using the full 3D model was set up in the

following way: To allow for a detailed elaboration of the stack performance, the controllable variables inlet temperature $T_{g,in}$, cell voltage E_{cell} and pressure p were selected to span a parameter space, which defines unique stack operation points. For each of these operation points in the selected parameter space, the considered objective function was maximized by tuning the air and reactant inlet flow rates. While the stack's produced, RU-averaged H_2 volume flux was set to be the main objective function, the stack's electrical efficiency (or rather specific electric energy demand per Nm^3 of produced H_2) was considered subsequently in the derivation of ideal stack operation windows from the created performance maps. The optimization procedure was conducted (i) by satisfying operation specifications, i.e. a fixed steam conversion and inlet composition, and (ii) by satisfying operation bounds, i.e. adhering to lower and upper bounds for the reactant and air flow rates as well as to a maximum tolerated 3D temperature gradient across the stack solid phase. The selected values and bounds for all the optimization parameters and constraints are discussed in detail in Section 3.3.2. While the inlet flow rates represent input parameters of the physical model, the steam conversion and the temperature gradient are model outputs. Thus, for each operation point within the parameter space spanned by the controllable variables, the reactant and sweep gas inlet flow rates were initially assumed, and then manually varied to maximize the objective function and fulfil the optimization constraints at the same time. Consequently, depending on the initial guess, multiple stack simulations needed to be conducted per operation point. To limit the computational requirements using the full 3D model for the two cell designs, increments of $\Delta T_{g,in} = 50$ K, $\Delta E_{cell} = 0.05$ V and $\Delta p = 5$ atm were considered reasonable to adequately screen the parameter space.

2.2. Experimental

The ESC (supplier: Kerafol®, Germany) and CSC (supplier: Elcogen® AS, Estonia) commercial cells have a total area of 19.63 cm^2 and an active surface area of 10.18 cm^2 (equal to the size of the anode area). Microstructural analyses of both cell types were performed using a scanning electron microscope (SEM, Quanta 200 by FEI) outfitted with an energy-dispersive x-ray spectroscopy (EDX) system. Micrographs of the two cell architectures recorded using SEM are depicted in Fig. 1.

In both cell designs, a gadolinium-doped ceria (CGO) barrier layer is applied between the mixed ion–electron conducting (MIEC) single-phase doped perovskite anode (lanthanum strontium cobalt ferrite (LSCF) for the ESC, lanthanum strontium cobaltite (LSC) for the CSC) and the doped zirconia electrolyte to prevent the formation of an insulating pyrochlore phase at the MIEC-electrolyte interface [55]. In case of the CSC, the Ni-YSZ cathode structure is divided into a relatively thin functional layer (fl) adhered to the central 8 mol % yttria-stabilized zirconia (denoted as YSZ) electrolyte and a more porous and thicker diffusion layer (dl). An additional CGO barrier layer separating the Ni-CGO cermet composite from the 3 mol% yttria-stabilized zirconia electrolyte (denoted as 3YSZ) is clearly distinguishable in case of the ESC to prevent secondary phase formation [39]. The elemental composition of all layers was determined using EDX area scans.

The electrochemical behavior of the cells was characterized using a custom-made open -flange setup manufactured by Fiaxell, which is placed inside an oven. The cells were mounted on a Ni plate supported by a Crofer casing. A Ni mesh was used for gas diffusion and current collection, and a thermiculite sheet ring as well as thermiculite paste for sealing between the cell's cathode and the Ni plate. At the air side, an Au grid is used as the current collector. The Crofer housing is equipped with pipes for the gas flows to and from the cell. The cathode was provided with a hydrogen/steam mixture through a tube leading to the center of the cell. Steam was generated by feeding liquid, deionized water with the flow rate being controlled by a Liquiflow-MFC directly into the hot hydrogen flow. By moving through the heated oven, the water evaporates before it reaches the cell surface. Two smaller pipes are placed towards the outside of the circular cell for the evacuation of the product gas. The anode compartment was connected to a gas inlet tube feeding compressed air as a sweep gas. As there is no sealing on the anode side, the sweep gas/product mixture escapes into the oven chamber. The Ni plate on the cathode side and the Au grid on the anode side were connected to an ADAM data acquisition system and electrical load for the electrochemical characterizations. Additionally, multiple thermocouples placed near the cell (~1 cm distance to the edge of the electrolyte) were employed to monitor the temperature during the experiments. Fig. 2a depicts a schematic of the test bench for the cell performance characterization, whereas Fig. 2b illustrates the model geometry that was applied for the single cell simulations.

To begin a test, the Ni-cermet anode was reduced by gradually switching the inlet gas from 3 SL h^{-1} N_2 to 3 SL h^{-1} H_2 at 900 °C. While an initial polarization curve in fuel cell mode was recorded at 800 °C, the experiment was switched subsequently to electrolysis mode by increasing the liquid water flow until an absolute humidity of 90% was reached in the feed. The cell performance was then assessed by recording polarization curves at various temperatures, 600–750 °C for the CSC and 700–900 °C for the ESC. The current density was increased with a rate of 0.01 A cm^{-2} s^{-1} up to the highest polarization respectively. Impedance data were obtained by running frequency domain sweeps (frequency range from 0.1 to 10000 Hz) under open-circuit conditions with an amplitude of 15 mV. The sweep was controlled by a Solartron 1287A potentiostat and the response measured by a frequency response analyzer (Solartron SI 1255).

3. Results and discussion

3.1. Model calibration and validation

3.1.1. Model parameters: Single cell level

As a first step, the multi-physics single cell model was parametrized

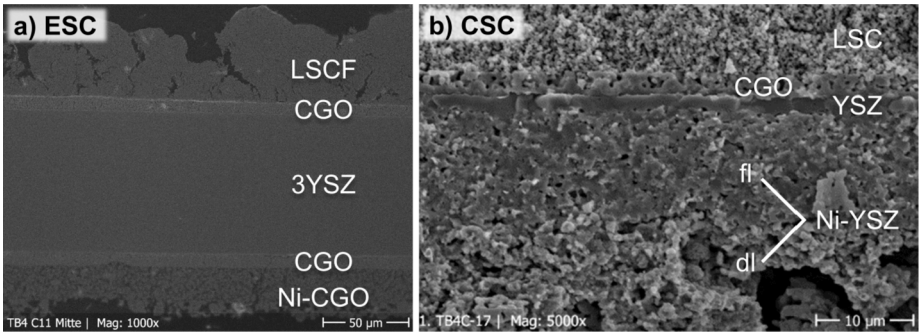

Fig. 1. Polished cross-sectional images of commercial SOC single cells with $A_{cell} = 10.18$ cm^2 obtained via SEM illustrating the MEA, i.e. porous electrode and dense electrolyte layers, of both cell designs. Ni-cermet electrodes were reduced in pure H_2 at 900 °C. a) ESC, Ni-CGO/CGO/3YSZ/CGO/LSCF, b) CSC, Ni-YSZ/YSZ/CGO/LSC. fl, functional layer; dl, diffusion layer.

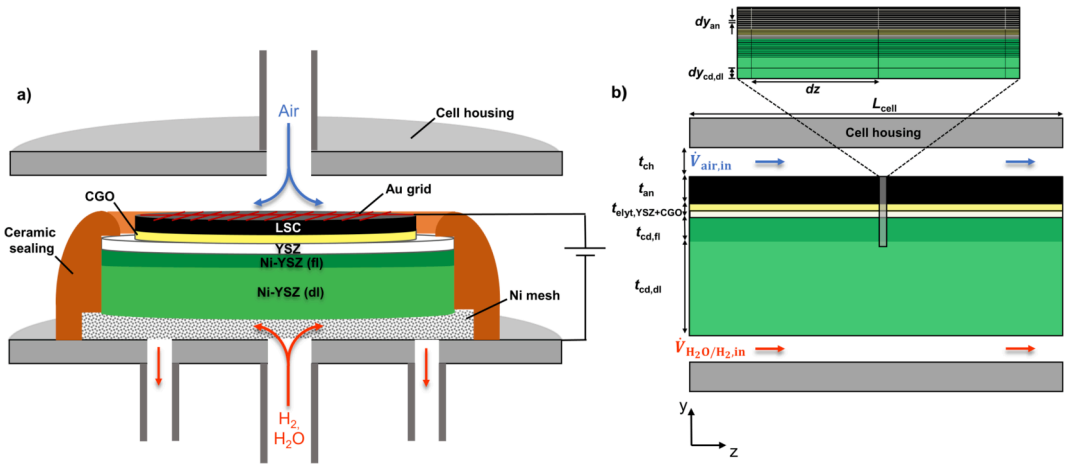

Fig. 2. a) Schematic of the test bench for the electrochemical performance characterization of the single cells and b) model geometry considered as computational domain with the true-to-scale numerical grid depicted as a zoom into the MEA. For the illustrated CSC design, the axial flow direction was discretized into 100 equidistant cells for the channel and MEA domains, and the radial direction across the thickness into 80 cells with varying heights.

comprehensively with respect to microstructural, thermal and conductance parameters. Table 1 compiles the acquired microstructural parameters including the layer thicknesses, mean particle diameters, solid phase volume fractions and porosities, alongside the physical dimensions of the cells.

Based on the extracted microstructural information, the pore diameters d_{pore}, volumetric triple-phase boundary lengths (TPBs) λ^{V}_{TPB}, as well as specific surface areas (double-phase boundaries, DPBs) of the electrode materials $A^{V}_{gas/ede}$ are evaluated by applying extended percolation theory [56–58], while the pore phase tortuosity factor $\tau_{fac,pore}$ is evaluated analytically as a function of the experimentally assessed porosity ϵ [59].

Table 2 compiles the material properties of the bulk solid phases entering the model, including the materials' ionic σ_{io} and electronic conductivities σ_{el}, along with their thermal properties.

For the MIEC materials, O_2-partial pressure dependent conductivity expressions are used in case of CGO ($Ce0.9Gd0.1O2_{-\delta}$), since the ceria-based material exhibits considerable σ_{el} under low p_{O_2} conditions in the cathode [63,64], while conductivity data for 6428-LSCF

Table 1
Model input parameters to reproduce the experimental single cell polarization and impedance data.

Parameter	Value		Reference
	CSC	ESC	
Active cell area, A_{cell}	10.18 cm^2		Experiment
Cell length, L_{cell}	1.8 cm		Experiment
Cell width, w_{cell}	5.65 cm		Calculated
Channel height, t_{ch}	1.0 mm		Estimate
Gas inlet temperature, $T_{g,in}$	600–750 °C	700–900 °C	Experiment
Absolute pressure, p	1 atm		Experiment
Gas inlet composition, $X_{H_2O/H_2,in}$	90%/10% H_2O/H_2		Experiment
H_2/H_2O inlet flow rate, $\dot{V}_{H_2O/H_2,in}$	44.0–171.6 NmL min^{-1}		Experiment
Air inlet flow rate, $\dot{V}_{air,in}$	114.5 NmL min^{-1}		Experiment
Cathode thickness (fl/dl), $t_{cd,\ fl(dl)}$	13 / 373 µm	25 / - µm	SEM
Anode thickness, t_{an}	15 µm	48 µm	SEM
CGO(cd)/Electrolyte /CGO(an) thickness, $t_{bl(cd)}/t_{elyt}/t_{bl(an)}$	- / 4 / 3 µm	7 / 81 / 7 µm	SEM
Cathode porosity (fl/dl), $\varepsilon_{cd,fl(dl)}$	0.22 / 0.36	0.30 / -	SEM
CGO layer porosity (cd/an), $\varepsilon_{bl,cd(an)}$	- / 0.14	0.20 / 0.23	SEM
Cathode mean particle diameter (fl/dl), $d_{p,cd,fl(dl)}$	0.9 / 0.9 µm	0.4 / - µm	SEM
Cathode Ni volume fraction (fl/dl), $\nu_{f,cd,fl(dl)}$	0.35 / 0.5	0.62 / -	EDX
Anode porosity, ε_{an}	0.29	0.20	SEM
Anode mean particle diameter, $d_{p,an}$	0.7 µm	0.4 µm	SEM

Table 2
Material properties.

	Value			Reference
Electrical properties				
Ni electronic conductivity, σ_{el}	3.27×10^4-$10.653 \times T$ S cm^{-1}			[60]
3YSZ ionic conductivity, σ_{io}	$37.8 \times e^{-8442/T}$ S cm^{-1}			[61]
YSZ ionic conductivity, σ_{io}	$3.34 \times 10^2 \times e^{-10300/T}$ S cm^{-1}			[62]
CGO ionic conductivity, σ_{io}	$(1.09 \times 10^5/T)\times e^{-7426.9/T}\times(1+\delta/0.05)$ S cm^{-1}			[63,64]
CGO electronic conductivity, σ_{el}	$(3.46 \times 10^9/T) \times e^{-28779/T}\times p_{O_2}{}^{-0.25}$ S cm^{-1}			[63]
Extra oxygen vacancies in CGO, δ	$1.3 \times 10^4 \times e^{-25530/T}\times p_{O_2}{}^{-0.25}$			[63]
LSCF electronic conductivity, σ_{el}	$983.25–0.627 \times T$ S cm^{-1}, $T > 923.15$ K			[65]
LSCF ionic conductivity, σ_{io}	$7.35 \times 10^4 \times e^{-14962/T}$ S cm^{-1}			[66]
LSC electronic conductivity, σ_{io}	$4860.1–2.98 \times T$ S cm^{-1}, $T > 923.15$ K			[67]
LSC ionic conductivity, σ_{io}	$1.31 \times 10^4 \times e^{-11274/T}$ S cm^{-1}			[68]
3YSZ-CGO contact resistance (ESC), $R_{contact,elyt\rightarrow bl}$	$2.09 \times 10^{-11} \times e^{118224/RT}$ Ω cm^2			Fitted
Thermal properties				
Bulk solid phase	Density (kg m^{-3})	Specific heat capacity (J kg^{-1} K^{-1})	Thermal conductivity (W m^{-1} K^{-1})	Reference
Ni	8850	549	66.2	[69–71]
YSZ or 3YSZ	5938	636	2.1	[72,73]
CGO	7210	521	0.98	[74–76]
LSCF	6300	608	3.25	[77,78]
LSC	6310	799	3.94	[78,79]

$(La_{0.6}Sr_{0.4}Co_{0.2}Fe_{0.8}O_{3-\delta})$ from Stevenson et al. [65] and Fan et al. [66] and for 64-LSC $(La_{0.6}Sr_{0.4}CoO_{3-\delta})$ from Søgaard et al. [67] and Teraoka et al. [68], all measured in air, were used at the anode side. For these materials, there exists a p_{O_2}-dependency of σ_{el} and σ_{io} due to oxygen vacancy concentration variations (while thermodynamic factors and chemical diffusion coefficients can often be reasonably assumed to be independent of pressure [80]). Still, the conductivities are set p_{O_2}-independent for LSCF and LSC here, due to the fact that high-pressure conductivity data for these perovskites are scarce in the literature (a −0.25 pressure exponent cannot be generally applied [67]). Instead, by

evaluating the polarization resistance $\log R_{pol}$ versus $\log p_{O_2}$ dependency from published EIS data [80,81], the influence of pressure on the anode performance is assumed to be lumped into the pressure-dependency of the exchange current density i_{0,O_2} solely (via the pressure exponent n_{O_2}), which provides sufficient accuracy for the purpose of this study.

The electrochemical model is calibrated by comparison with experimental data, as discussed in Section 3.1.2. To reduce the amount of tuneable kinetic fit parameters and to facilitate a physical soundness of the electrochemical parametrization, all the activation energies E_r (with r representing the charge transfer (CT)-reaction index) and the pressure exponents n_k (k denoting the species index) of the exchange current density $i_{0,r}$ were acquired from EIS data from literature for all the different cell materials. Therefore, comprehensive symmetrical cell measurements conducted on thin electrodes to minimize mass transport limitations reported by Riegraf et al. [82] were used to set the kinetic parameters for Ni-CGO, who found a low reaction order dependency with respect to both H_2 and H_2O, while full cell data from the work of Leonide et al. [83], who determined the B-V parameters and the contributions from anode and cathode independently from each other, were used for Ni-YSZ and to define $E_{O_2,LSCF}$. Still, $n_{O_2,LSCF} = 0.11$ was set according to the value found by Railsback et al. [80] due to high-pressure measurements ($p_{O_2} = 0.1$–10 atm). Lastly, for LSC, impedance data from Lu et al. [81] ($T = 650$–750 °C, $p_{O_2} = 0.1$–1 atm) were evaluated to define the kinetic parameters of the CSC anode material, yielding $E_{O_2,LSC} = 150$ kJ mol^{-1} and $n_{O_2,LSCF} = 0.22$. On this basis, only the pre-exponential factors A_r and the anodic CT coefficients β_a, (β_c were taken as $1 - \beta_a$) of the half-cell reactions were treated as fit parameters. With respect to the different CT pathways to establish the B-V framework for the individual electrode materials, it is assumed that the H_2O reduction occurs via the TPB pathway in case of Ni-YSZ [84], so that λ^V_{TPB} is used to evaluate the Faradaic current density i^V_F (see Table S1). However, since there is strong evidence from experimental and modeling studies that in the case of typical Ni-CGO cermet microstructures, the DPB-mechanism is prevailing over the TPB-pathway due to the MIEC properties of CGO [85], $A^V_{gas/CGO}$ is used in charge balance for this material. The volumetric surface area $A^V_{gas/ede}$ is used to calculate i^V_F in case of the single-phase MIEC anode materials, in line with the model assumptions (see Section 2.1).

3.1.2. Comparison of experimental data with simulations

In Fig. 3a-b depicts the modelled polarization curves reproducing the experimental data for both cell designs, which were recorded at atmospheric pressure, $T = 600$–900 °C, supplying a mixture of 90%/10% H_2O/H_2 and air to the gas channels.

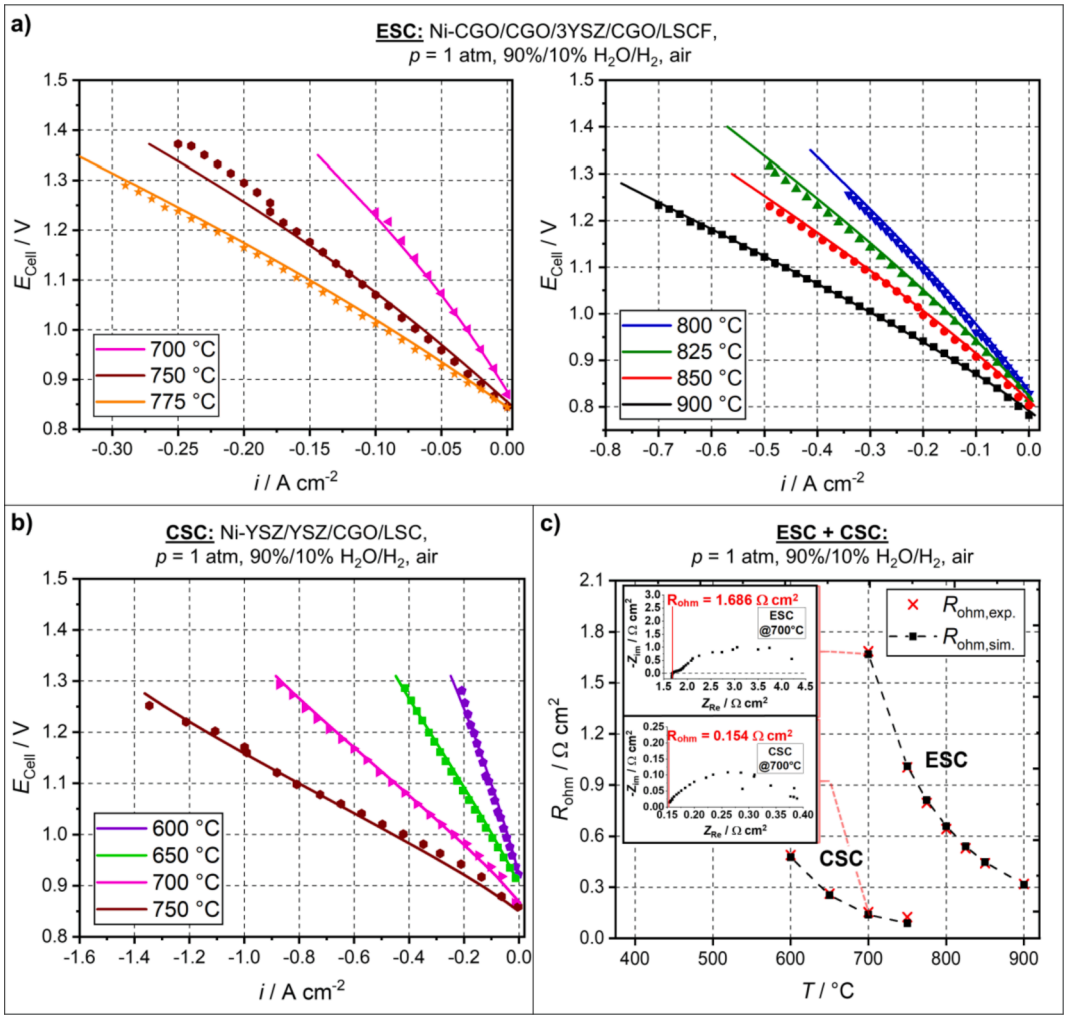

Fig. 3. (a-b) Comparison between 2D adiabatically simulated (continuous) and experimentally recorded (dotted) steady-state polarization curves of commercial SOC single cells ($A_{cell} = 10.18$ cm^2) for a) the ESC design and b) the CSC design. Operation conditions: $T_{g,in} = 600$–900 °C, $p = 1$ atm, 90%/10% H_2O/H_2, $\dot{V}_{H_2O/H_2,in} = 76.6$ NmL min^{-1} (ESC), $\dot{V}_{H_2O/H_2,in} = 44.0$–$171.6$ NmL min^{-1} (CSC), 114.5 NmL min^{-1} air. c) Comparison between simulated (dash-dotted) and measured (colored) ohmic resistances R_{ohm} for both cell designs at different temperatures. As indicated in the figure, experimental R_{ohm} were extracted from EIS measurements as HF intercepts at OCV.

The measurement conditions during the electrochemical characterization procedure are listed in Table 1. After having calibrated the fit parameters, the simulated polarization curves agree with the experimental data nearly quantitatively for both cell types over the entire temperature range, aside from an offset at $E_{cell} > 1.25$ V for the ESC polarization curve at 750 °C in Fig. 3a. The origin of this offset couldn't be pinpointed unambiguously from the experiments; however, since it only appeared for this specific measurement, it didn't impact the calibration procedure, and with that, all the further calculations performed in the following sections. Interestingly, the shape of the polarization curves of the ESC and the CSC do not differ very much, with a more pronounced concave shape of the curves pertaining to the ESC, and a nearly linear course of the CSC polarization curves. A convex-shaped diffusion arc in the high current density region related to mass transport losses across the Ni-YSZ support layer starts to appear for the simulated curve at 750 °C at ~1.35 A cm^{-2} ($SC \sim 80\%$), but cannot be clearly identified from the experimental data, indicating a well-percolated pore phase network providing sufficient gas supply ($\varepsilon_{Ni-YSZ,\,dl} \sim 0.36$) to the electrochemically active sites. Notably, due to the small cell active areas, the 2D thermal model predicts a rather limited temperature development due to electrochemistry and irreversible Joule heating, with a maximum temperature increase of ~3 K for the ESC at 1.37 V, 750 °C. Near-isothermal conditions ($\Delta T < 5$ °C during all measurements) were also verified by continuously monitoring the temperature via thermocouples.

Additionally, the ohmic resistances of the single cells R_{ohm} have been extracted via electrochemical impedance spectroscopy (EIS) as high frequency (HF) intercepts at open circuit voltage (OCV). A comparison of the experimental values with the simulated R_{ohm} is depicted in Fig. 3c. In case of the ESC, the experimental R_{ohm} values were always higher than the calculated sum of the individual cell layers without interfacial contributions, such that an additional contact resistance $R_{contact,elyt\rightarrow bl}$ was implemented into the model for this cell configuration (Table 2). Solid-state reactions and diffusion processes during co-firing of YSZ and CGO are well-known [55,83], so that this resistance contribution can be reasonably attributed to an O_2 transfer resistance across the two YSZ-CGO interfaces. Indeed, the resistance was found to follow an Arrhenius-type temperature dependency (cf. Fig. 3c), with a fitted activation energy of ~118 kJ mol^{-1}, which is in the range of values obtained from conductivity measurements of YSZ-CGO interdiffusion layers (~111 kJ mol^{-1} [86]). For the CSC, the model slightly underestimates R_{ohm} at the highest temperature considered, 750 °C, possibly due to additional ohmic loss contributions not accounted for in the model (e.g. interdiffusion zones, grain boundary resistances or low-conductance impurities), but other than that, quantitatively reproduces the measured values. As can be verified from Fig. 3c, R_{ohm} is notably higher for the ESC compared to the CSC as expected (~0.3 Ω cm^2 at 900 °C for the ESC and at 650 °C for the CSC), dominated by the large resistance of the ~81 µm 3YSZ electrolyte.

In total, the agreement between model and the experiments is considered to be satisfactory, particularly with respect to the low number of tunable fit parameters. Table 3 compiles the kinetic parameters acquired for each electrode material from the electrochemical characterization, which are used as a basis for the further simulations performed in Section 3.2 and 3.3.

3.1.3. Pressurized operation

For PtM plant concepts, pressurized operation of system-integrated SOEC stacks is of high interest, since the catalytic methanation unit operates at elevated pressures, and in turn, steam at a pressure level of ~10–50 bar is produced in its liquid cooling system, which in coupled operation represents the steam fed to the electrolyzers [9]. Thus, a cost-effective system integration can be promoted if drastic expansion steps of the steam produced in the cooling system are avoided, thereby saving at least parts of the compression costs of the electrolytic H_2 entering the methanation unit. In order to validate the model under pressurized operation conditions, experimental single cell data from the work of Bernadet et al. [29] conducted on CSCs were considered. These cell tests were chosen due to the following reasons: (i) Both Ni-YSZ and LSCF electrode materials are contained in the cell design, so that aside from the pre-exponential factors A_r, the kinetic parameters as extracted before can be rationally used without refitting, which significantly reduces the amount of unknown fit parameters, and (ii) microstructural information are reported, which further minimizes the amount of parameters that need to be estimated, such that the risk of overfitting the data is reduced. Table 4 lists the model input parameters reproducing the cell measurements at $p = 1$–10 bar and $T = 800$ °C, feeding 35/58.5/6.6 $N_2/H_2O/H_2$ (corresponding to a fraction of 90/10 H_2O/H_2) and air, while the comparison of simulated against experimental polarization curves is shown in Fig. 4.

Table 3
Kinetic fit parameters acquired from the model calibration and validation procedure.

Parameter	Value	
Anode materials	Ni-CGO	Ni-YSZ
Exchange current density, i_{0,H_2O}	$5.9 \times 10^3 \times e^{-\frac{111900}{R/T}} \times p_{H_2}^{0.01} \times p_{H_2O}^{0.08}$ A cm^{-2}	$0.68 \times e^{-\frac{105000}{R/T}} \times p_{H_2}^{-0.1} \times p_{H_2O}^{0.33}$ A cm^{-1}
Anodic charge transfer coefficient, β_a	0.75	0.6
Cathodic charge transfer coefficient, β_c	0.25	0.4
Cathode materials	LSCF	LSC
Exchange current density, i_{0,O_2}	$8.5 \times 10^2 \times e^{-\frac{139000}{R/T}} \times p_{O_2}^{0.11}$ A cm^{-2}	$7.6 \times 10^5 \times e^{-\frac{150000}{R/T}} \times p_{O_2}^{0.22}$ A cm^{-2}
Anodic charge transfer coefficient, β_a	0.5	0.65
Cathodic charge transfer coefficient, β_c	0.5	0.35

Units of partial pressures are given in atm.

For additional simplicity, the unreported particle diameters d_p were set to the experimentally assessed d_{pore}, while a channel height of 1 mm is assumed to calculate the inlet velocity from the volumetric flow rates. As apparent from the plots, the model reproduces the experimental data with good accordance. Clearly, the increase of the OCV with pressure, alongside the shift of the limiting current density during pressurized operation at 10 bar are both reproduced correctly, leading to a crossing of the two curves at a steam conversion of $SC \sim 50\%$. Crucially, the fitting of the pre-factors, which is mandatorily required due to the unique cell microstructure, the sintering conditions, the polarization prehistory, etc., cannot be responsible for predicting the features associated with operation at elevated pressures, since A_r is pressure-independent. This verifies that the influence of pressure on porous medium gas transport [29,30] and the charge transfer kinetics in the model (see Table S1) in the model are in line with the experimental data, and thus, leads to a high degree of confidence in the model's soundness and applicability for the further simulations including pressurized operation conditions.

3.2. Single cell performance analysis

Having calibrated the model, the next step is to comprehensively analyze single cell performance by varying key controllable variables in a parametric study. The reactant mixture supplied to the cathode is not considered to be controllable, and fixed at 90%/10% H_2O/H_2, considering a minimum of 5–10% H_2 is required in the inlet stream to prevent the Ni particles in the cermet electrode from re-oxidation [9,19]. Similarly, while $\dot{V}_{air,in}$ is a key operating parameter on stack-scale due to the temperature development, the influence on single cell level is limited, so

Table 4
Model input parameters for reproducing pressurized single cell tests from Bernadet et al. [29].

Parameter	Value	Reference
Active cell area, A_{cell}	3.14 cm^2	[29]
Cell length, L_{cell}	1.0 cm	[29]
Cell width, w_{cell}	3.14 cm	[29]
Channel height, t_{ch}	1.0 mm	Estimate
Gas inlet temperature, $T_{g,in}$	800 °C	[29]
Absolute pressure, p	1–10 bar	[29]
Gas inlet composition, X_{in}	35%/58.5%/6.5 % $N_2/H_2O/H_2$	[29]
Cathode / Anode inlet flow rate, $\dot{V}_{in}$	58.0 / 115.9 NmL min^{-1}	[29]
Contact resistance, $R_{contact}$	0.159 Ω cm^2	[29]
Cathode thickness, t_{cd}	260 µm	[29]
Anode thickness (LSCF/LSC), t_{an}	30 / 20 µm	[29]
YSZ/CGO(an) thickness, $t_{elyt}/t_{bl,an}$	5 / 4 µm	[29]
Cathode porosity, ε_{cd}	0.25	[29]
Cathode mean particle diameter, $d_{p,cd}$	0.8 µm	Estimate
Cathode Ni volume fraction, $\nu_{f,cd}$	0.5	Estimate
Cathode tortuosity factor, $\tau_{fac,cd}$	15	[29]
Cathode mean pore diameter, $d_{pore,cd}$	0.8 µm	[29]
Anode porosity, ε_{an}	0.34	[29]
Anode mean particle diameter, $d_{p,an}$	1.0 µm	Estimate
Anode tortuosity factor, $\tau_{fac,an}$	10	[29]
Anode mean pore diameter, $d_{pore,an}$	1.0 µm	[29]
Cathode pre-exponential factor, A_{H_2/H_2O}	1.42 A cm^{-1} $atm^{-0.23}$	Fit
Anode pre-exponential factor, A_{O_2}	5.3 × 10^5 A cm^{-2} $atm^{-0.11}$	Fit

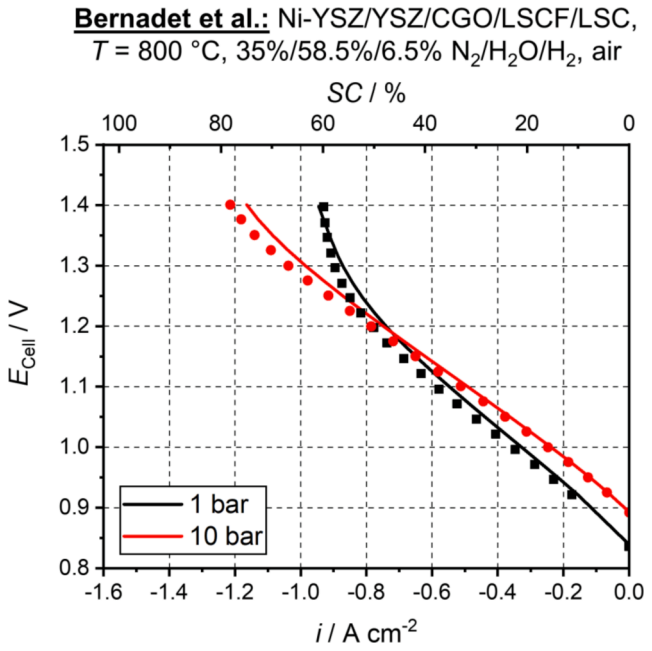

Fig. 4. 2D adiabatically simulated (continuous) polarization curves reproducing experimental data (dotted) from the work of Bernadet et al. [29] recorded at $T = 800$ °C, $p = 1$–10 bar, supplying 35%/58.5%/6.5 % $N_2/H_2O/H_2$ and air to a cathode-supported Ni-YSZ/YSZ/CGO/LSCF/LSC cell ($A_{cell} = 3.14$ cm^2).

that a constant $\dot{V}_{air,in} = 1.5 \times \dot{V}_{H_2O/H_2,in}$ was fixed here to reach an excess air ratio Ψ_{air} of ~1, with Ψ_{air} being defined according to.

$$\Psi_{air} = \frac{\dot{n}_{O_2,in}}{\dot{n}_{O_2,out} - \dot{n}_{O_2,in}} \tag{2}$$

where $\dot{n}_{O_2}$ is the molar flux of oxygen. The controllable variables comprise the inlet gas temperature $T_{g,in}$, the absolute pressure p, the cell voltage E_{cell}, and inlet flow rate $\dot{V}_{H_2O/H_2,in}$, with their lower and upper bounds listed in Table 5 respectively.

To assess the performance of the single cells, the metrics under consideration are (i) the produced H_2 volume flux, $\dot{V}_{H_2}$ and (ii) the electrolysis efficiency based on the lower heating value (LHV), which can either be calculated with respect to the total (heat + electrical) energy input (Eq. (3)) or with respect to the electrical energy input only (Eq. (4)).

$$\eta_{LHV} = \frac{\left(\dot{m}_{H_2,out} - \dot{m}_{H_2,in}\right) LHV_{H_2}}{w_{cell} E_{cell} \int_0^{L_{cell}} i dz + \sum_{ch} \dot{m}_{ch,in} \int_{T_\infty}^{T_{ch,in}} C_{p,g,ch} dT} \tag{3}$$

$$\eta_{elec,LHV} = \frac{\left(\dot{m}_{H_2,out} - \dot{m}_{H_2,in}\right) LHV_{H_2}}{w_{cell} E_{cell} \int_0^{L_{cell}} i dz} \tag{4}$$

Here, $\dot{m}$ is the mass flux, w_{cell} and L_{cell} are the cell's width and length, i the local current density, z the axial coordinate, and $C_{p,g,ch}$ the specific heat capacity of the gas phase in channel ch. The reference temperature is set to ambient conditions ($T_\infty = 25$ °C). Obviously, the SOEC operation is not intended for stand-alone operation without thermal integration, so that efficiencies higher than η_{LHV} will be reached in practice, with $\eta_{elec,LHV}$ being the theoretical maximum that can be achieved. Still, during the intended coupled plant operation, electrical heaters will most likely be required at least temporarily to heat the SOEC inlet streams, in particular when the stack is not operated exothermally producing a significant amount of excess heat [9,19], which is due to unavoidable heat losses of all plant components and pipes, non-ideal and finite-area heat exchangers etc. Thus, it is expected that an efficiency definition that contains the information that a certain amount of energy proportional to $\dot{m}_{in}$ is required to heat the inlet streams will be relevant on system scale despite thermal integration.

Fig. 5 depicts 3D contour maps illustrating the performance of the ESC design, which were obtained by conducting parametric 2D adiabatic simulations.

In this representation, the electrolysis efficiency is given by the vertical axis, the produced H_2 volume flux $\dot{V}_{H_2}$ is included via the colour gradients, whereas the isolines correspond to the steam conversion. From Fig. 5a, it can be clearly extracted that $\dot{V}_{H_2}$ is maximized at high E_{cell} and $\dot{V}_{H_2O/H_2,in}$, though for the efficiency, the trend analysis is more intricate: While $\eta_{elec,LHV}$ is linearly decreasing with E_{cell} and not a function of SC at constant E_{cell} (cf. Fig. 5b), η_{LHV} is increasing by enhancing the steam conversion up to $SC \sim 80\%$, which represents a threshold value in the proportionality. Surpassing the threshold SC leads to

Table 5
Lower and upper Bounds of controllable variables for single cell parametric studies.

Controllable variable	Bounds	
	ESC	CSC
Gas inlet temperature, $T_{g,in}$	750–850 °C	650–750 °C
Absolute pressure, p	1–20 atm	
Cell voltage, E_{cell}	1.2–1.45 V	
H_2/H_2O inlet flow rate[a], $\dot{V}_{H_2O/H_2,in}$	0.7–7.9 NL h^{-1}	2.4–21.5 NL h^{-1}

[a] Set to reach SC ~25% at minimum and ~100% at peak operation points.

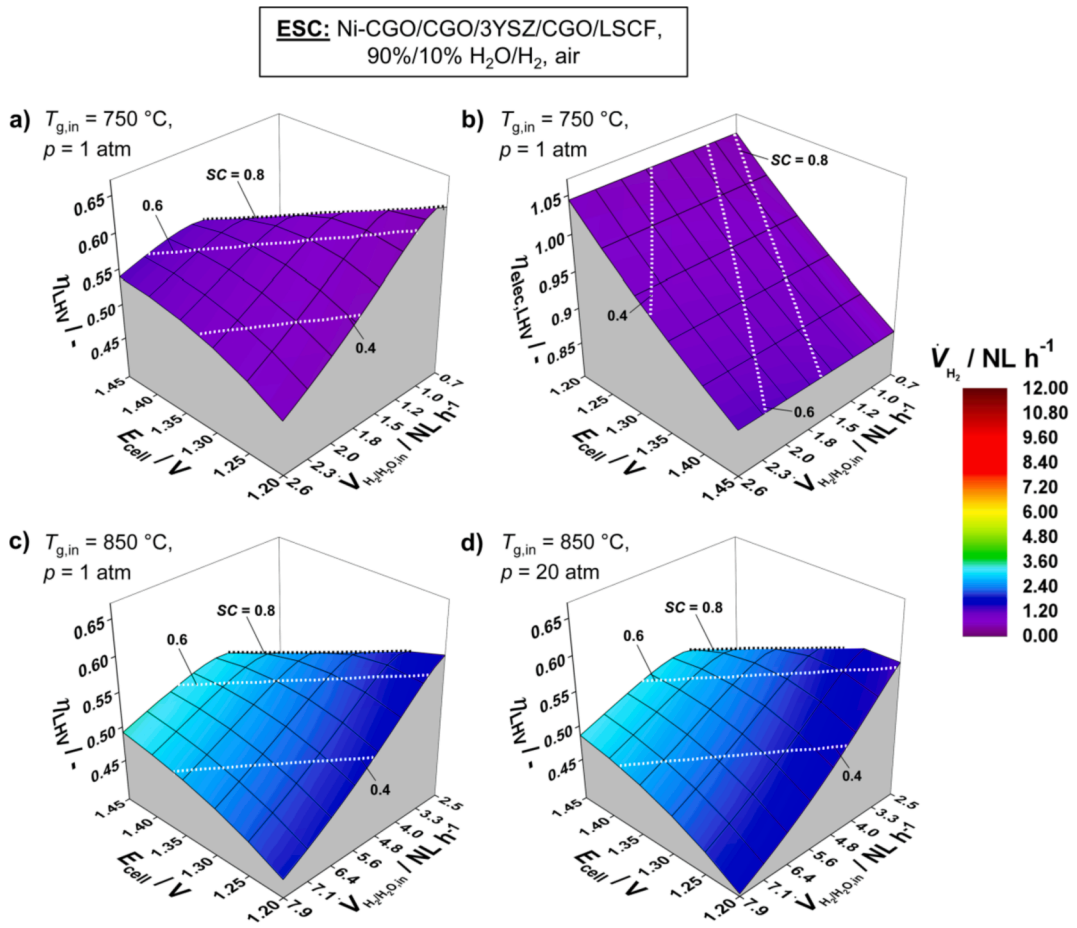

Fig. 5. (a-d) 3D contour maps of the ESC design illustrating cell performance in selected parameter spaces. A single map was created by performing 2D adiabatic single cell simulations by varying $\dot{V}_{H_2O/H_2,in}$ and E_{cell}. Operation conditions: 90%/10% H_2O/H_2, $\dot{V}_{air,in} = 1.5 \times \dot{V}_{H_2O/H_2,in}$, $E_{cell} = 1.2$–1.45 V (a-b) 750 °C, $p = 1$ atm, c) 850 °C, $p = 1$ atm, d) 850 °C, $p = 20$ atm.

efficiency losses due to the creation of reactant starvation zones across the electrodes, i.e. concentration gradients, which make the electrical work input and inlet stream heating requirement overcompensate the useful chemical H_2 output [15]. Clearly, by comparing Fig. 5a, c and d, it can be deduced that the threshold *SC* is not a function of the temperature, cell voltage or pressure, and thus can be used to estimate when reactant shortage could practically worsen the overall PtM system efficiency [19]. Moreover, for the ESC design, a pressure increase to 20 atm leads to cell-level performance decreases, which is apparent by comparing Fig. 5c and d. The increase of the OCV under pressurized conditions (~73 mV at 850 °C) cannot be compensated by decreased activation and concentration losses, since R_{ohm} represents an overwhelming fraction of the total resistance (Fig. 3c), which is not influenced by the absolute pressure. This is directly in line with the experimental results from Riedel et al. [41,87], who determined the electrochemical performance of an ESC-based 10-cell stack (with an equivalent layer composition as considered in this study) under pressurized conditions. For example, at a selected operation point at 850 °C, 1.35 V, *SC* = 80% and 20 atm, the ESC produces a volumetric H_2 flux of ~2.27 L h^{-1}, which corresponds to a decrease of ~9% compared to atmospheric pressure.

Fig. 6 presents the performance maps of the CSC-design in an equivalent depiction as in case of the ESC, with the controllable variables compiled in Table 5.

Unambiguously, the threshold *SC* for this cell design shifts to a lower value of ~75% (compared to ~80% of the ESC), which is a direct consequence of the mass transport resistance across the ~370 µm thick Ni-YSZ support and the relatively dense ($\varepsilon \sim 0.22$) functional layer, compared to the thinner and more porous ($\varepsilon \sim 0.3$) single Ni-CGO layer in case of the ESC, so that the impact of high reactant conversion on the performance is more severe for the CSC. However, a quantitative confrontation between the two cell designs with respect to the performance metrics showcases the merits of the CSC, which reaches a significantly better performance even when operating at distinctly lower temperatures. For example, at operation points of high $\dot{V}_{H_2}$ at $p = 1$ atm in the parameter spaces of Figs. 5 and 6, i.e., $E_{cell} = 1.45$ V and at a constant *SC* of ~55%, the CSC reaches $\dot{V}_{H_2} \sim 3.27$ NL h^{-1} at 650 °C, which is nearly equivalent to the produced H_2 output of 3.34 NL h^{-1} for the ESC at $\Delta T_{g,in} = 850$ °C. Yet, due to the lower inlet temperature, the CSC operates at $\eta_{LHV} \sim 58\%$ while the ESC only reaches ~51% efficiency. In turn, at a given $T_{g,in}$ of 750 °C, the CSC produces up to ~10.6 NL h^{-1} H_2, whereas the ESC only reaches approximately a tenth of this production rate, ~1.24 NL h^{-1}, with both operating at $E_{cell} = 1.45$ V and *SC* ~ 55%. Moreover, by comparing Fig. 6c and d, it is evident that pressurized operation conditions increases cell-level performance in case of the CSC. At 20 atm, the CSC reaches up to $\dot{V}_{H_2} \sim 11.7$ NL h^{-1} H_2, i.e., an enhancement of ~8% compared to operation at atmospheric pressure. This is related to (i) the faster charge transfer kinetics under pressure for both electrode materials, Ni-YSZ and LSC (see reaction orders in Table 3), and (ii) to the densified gas phase, which decreases concentration losses across the electrodes [29]. Not only the performance increase of the CSC design itself, but also its magnitude as predicted by the model agree very well with the pressurized CSC-design short-stack measurements from Riedel et al. [41], who e.g. found a current density increase of ~8% at 8 bar compared to 1.4

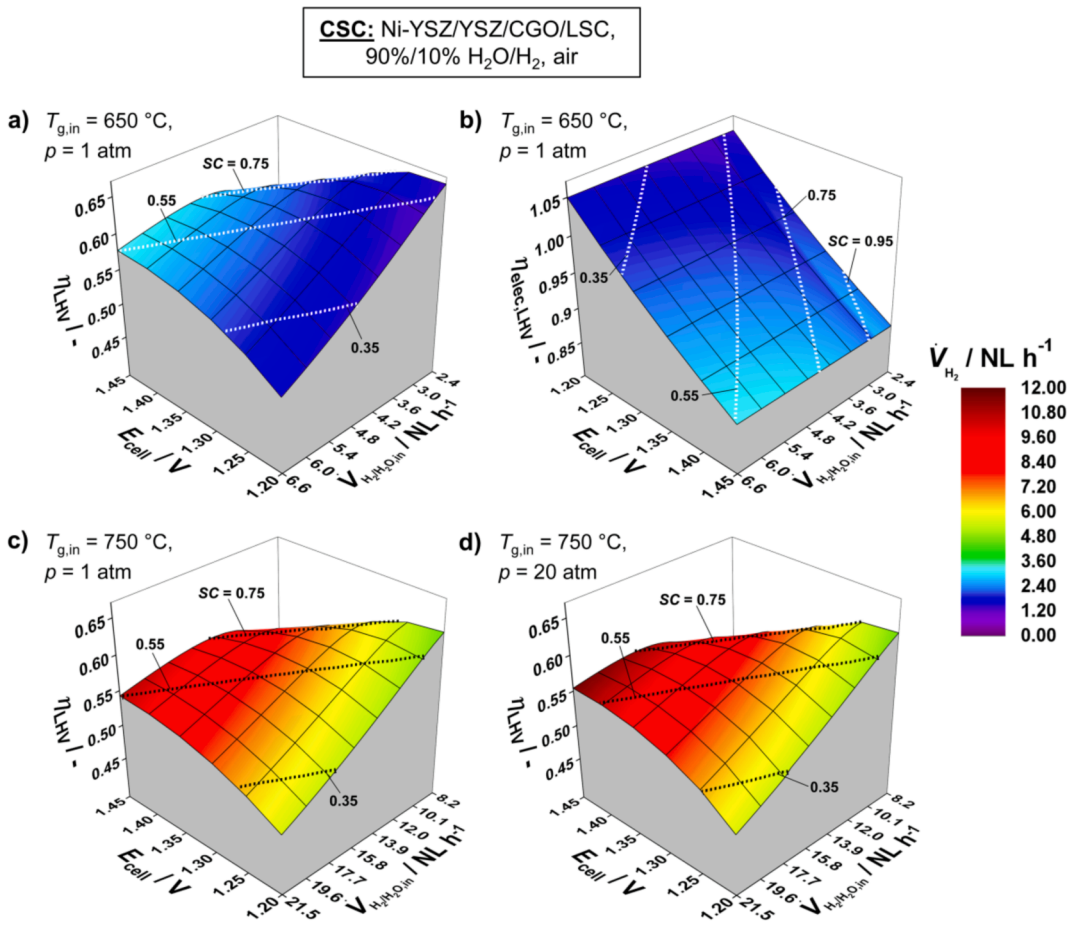

Fig. 6. (a-d) 3D contour maps of the CSC design illustrating cell performance in selected parameter spaces. Maps were created by performing 2D adiabatic single cell simulations by varying $\dot{V}_{H_2O/H_2,in}$ and E_{cell}. Operation conditions: 90%/10% H_2O/H_2, $\dot{V}_{air,in} = 1.5 \times \dot{V}_{H_2O/H_2,in}$, E_{cell} = 1.2–1.45 V (a-b) 650 °C, p = 1 atm, c) 750 °C, p = 1 atm, d) 750 °C, p = 20 atm.

bar under similar operation conditions (80%/20% H_2O/H_2, 750 °C, 1.4 V). Thus, due to the opposing trends of the cell performance versus pressure, it can be concluded that there exists a specific advantage of the CSC over the ESC design, which could be practically impactful for PtM applications when pressurized operation conditions of the SOEC module are considered to facilitate heat integration with the catalytic methanation unit [10,16,19]. This advantage is a direct consequence of the two cell types' largely different resistance contributions to their individual ASR values.

3.3. Stack-scale performance optimization

3.3.1. Model parameters: Stack level

There exist large physical differences between a single cell for lab-scale testing purposes and a commercial-scale stack, which requires the adjustment and extension of the simulation parameter configuration when performing a scale up to the 3D stack level. While the kinetic and microstructural parameters of the MEA for both cell designs were kept as extracted on single cell basis, additional simulation parameters on stack-scale involve the geometrical data and bulk material properties of the stack's peripheral insulation layer alongside the metallic interconnects forming the bipolar channel structure, aside from the enlarged cell dimensions. All the additional or adjusted model parameters with respect to the stack simulations are compiled in Table 6.

To perform application-oriented simulations, the Sunfire/Staxera® Mk200 design is used as a reference in this study [88], which represents a 30-cell stack unit that can be flexibly scaled to realize larger stack tower sizes for enhancing power capacities. For this design, the active cell area is 128 cm^2, subdivided into 24 channels [88], while the number of cells is set to 150 for the modeling purposes in this study, in order to simulate a commercially relevant industrial-scale stack concept in the > 10 kW-class [14]. Fig. 7 depicts front-views of the ESC and CSC RUs, as well as the corresponding stack layouts illustrating all the geometrical details and the stack components' arrangement.

A high-performance microporous silica-based insulation board is uniformly implemented at the stack's edges with 5 cm thickness (Table 6) [93]. Details regarding the stack's heat loss model involving natural convective and radiative heat exchange with the surroundings are provided in Table S2. A Ni mesh is used for contacting the cathode with the interconnects in both cell configurations, while at the anode side LSCF (ESC) and LSC (CSC) contact layers with individual protective coatings and resistance data are considered (Table 6) [89,90].

Comparing RU and single cell performances, it should be noted that aside from the performance losses in the RU due to the non-optimal contacting with the interconnects (cf. Table 6), the model assumptions (Section 2.1) imply an additional performance reduction of 25% due to applied channel/interconnect rib geometry, since in-plane diffusion underneath the interconnect ribs is not considered (cf. Section 2.1.1). Given that $w_{ic,rib}/2 = 750$ µm, this assumption should largely hold true in case of the ESC design (t_{cd} = 25 µm), while it represents a limitation for the CSC design, due to its relatively thick support layer ($t_{cd,fl+dl}$ = 386 µm). However, also considering additional factors that can affect stack level performance which are not being explicitly resolved with the present modelling approach, i.e., sealing effectiveness or uneven flow distributions caused by the manifolds/headers, the performance discrepancy accounted for in the model when moving from the single

Table 6
Additional or adjusted model input parameters for stack simulations.

Parameter	Value	Reference
Active cell area, A_{cell}	128 cm^2	[88]
Active cell length, L_{cell}	9 cm	[88]
Active cell width, w_{cell}	14.2 cm	[88]
Number of channels per layer, n_{ch}	24	[88]
Channel height, t_{ch}	1.0 mm	[88]
Cell width, w_{cell}	5.9 mm	[88]
Interconnect rib width $w_{ic,rib}$	1.5 mm	Estimate
Interconnect thickness, t_{ic}	0.5 mm	[88]
Number of cells in stack, n_{cell}	150	Simulation
Porous Promalight®-1000X insulation layer thickness, t_{ins}	5 cm	Simulation
Crofer® 22 APU-$MnCo_{1.9}Fe_{0.1}O_4$ coating-LSCF contact resistance, $R_{contact,ic\rightarrow an}$	$5.44 \times 10^{-6} \times e^{8492.6/T}$ Ω cm^2	[89]
Crofer® 22 APU-Ce/Co coating-LSC contact resistance, $R_{contact,ic\rightarrow an}$	0.0125 Ω cm^2	[90]
Crofer® 22 APU-Ni mesh contact resistance, $R_{contact,ic\rightarrow cd}$	0.01 Ω cm^2	[91]
Crofer® 22 APU emissivity	0.6	[92]
Electrode emissivity, $\varepsilon_{rad,ede}$	0.8	[92]
Porous Promalight®-1000X emissivity, $\varepsilon_{rad,ins}$	0.5	Estimate

Thermal properties

Solid phase	Density (kg m^{-3})	Specific heat capacity (J kg^{-1} K^{-1})	Thermal conductivity (W m^{-1} K^{-1})	
Crofer® 22 APU	7700	660.0	24.0	[91]
Porous Promalight®-1000X	280.0	1070	0.0295	[93]

cell to the planar RU/stack geometry generally compares well against experimental measurements: For example, considering the comparative polarization data of state-of-the-art CSC single cells and short-stacks performing steam electrolysis under similar conditions as in this study, compiled in the work of Wang et al. [16], a ~25–35% lowered current density in case of the RU (i.e., with interconnects) compared to the single cell can be identified (90%/10% H_2O/H_2, 700–800 °C, E_{cell} from OCV to ~1.3 V, 12 sccm cm^{-2} reactant flow rate). This compares very well against the ~30–35% performance reduction (depending on the temperature) accounted for in the model here due to the combined effect of (i) concentration losses underneath the ribs and (ii) the additional electrode-interconnect contact resistances.

The effective thermal properties of the lumped stack solid phase [49] are calculated based on the procedure previously published by Banerjee et al. [15] (see also Table S1). Most notably, individual thermal resistance networks for axial and radial conduction pathways are evaluated to calculate λ^{eff}_{stack}, accounting for (i) heat conduction through the solid components and (ii) radiative heat exchange between interconnects and electrodes [94].

3.3.2. Optimization study

The stack-scale optimization study was conducted with the full 3D-model and with the problem definition and numerical solution procedure described in Section 2.1. All the considered simulation parameters with their bounds are listed in Table 7.

A fixed *SC* of 80% was considered as a compromise between (i)

Table 7
Simulation parameters with their specifications and bounds for stack optimization study.

Parameter	Bounds or Specification	
	ESC	CSC
Steam conversion, *SC*	80%	
Gas inlet composition, $X_{H_2O/H_2,in}$	90%/10% H_2O/H_2	
Maximum temperature gradient, $\lvert\nabla T\rvert_{max}$	< 10 K cm^{-1}	
H_2/H_2O inlet flow rate, $\dot{V}_{H_2O/H_2,in}$	< 25 sccm cm^{-2}	
Air inlet flow rate, $\dot{V}_{air,in}$	$1\times\dot{V}_{H_2O/H_2,in} \leq \dot{V}_{air,in} \leq 6\times\dot{V}_{H_2O/H_2,in}$	
Gas inlet temperature, $T_{g,in}$	800–900 °C	650–750 °C
Absolute pressure, *p*	1–20 atm	
Cell voltage, E_{cell}	1.2–1.45 V	

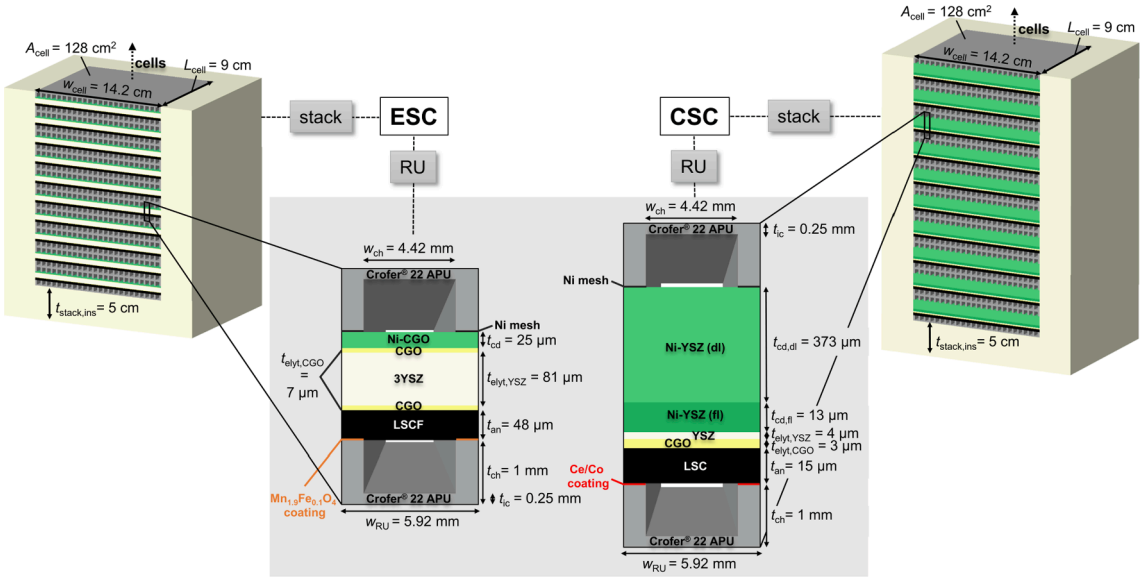

Fig. 7. Front-views of the ESC and CSC RUs and corresponding stack layouts as they are represented in the model. Note that the front axial insulation layer of the stack is not depicted due to illustrational purposes, and that the figure is not a true-to-scale representation.

concentration losses across the porous electrodes due to the formation of reactant starvation zones (cf. Section 3.2) and the associated risk of accelerated cell degradation due to high local overpotentials, and (ii) the heat integration with the catalytic methanation reactor on PtM system scale. Therein, to enable a high level of heat integration and importantly, to prevent electrical steam evaporation at the SOEC inlets, a high steam conversion at this level is required to produce sufficient heat via the exothermic methanation reaction [9,19]. This parameter selection is also in line with assumptions in other modelling studies [10] and thus, is used to reasonably limit the parameter space for the stack optimization study. The inlet composition has been fixed at 90%/10% H_2O/H_2 for the same reasons as stated in Section 3.2, i.e., redox stability of the cathode by ensuring a sufficiently reducing atmosphere. The maximum 3D-temperature gradient across the stack solid phase $|\nabla T|_{max}$ is an important control parameter with respect to the thermal management of the stack, and set to a maximum of 10 K cm^{-1} as proposed by Aguiar et al. [95], to avoid the occurrence of detrimental steep temperature gradients across the cell components, and is defined according to Eq. (5),

$$|\nabla T|_{max} = max\left(\sqrt{\left(\frac{\partial T_{stack,s}}{\partial x}\right)^2 + \left(\frac{\partial T_{stack,s}}{\partial y}\right)^2 + \left(\frac{\partial T_{stack,s}}{\partial z}\right)^2}\right) \quad (5)$$

where x, y and z are the spatial coordinates, and $T_{stack,s}$ the stack solid phase temperature (not including insulation). The upper bound for the inlet flow rate $\dot{V}_{H_2O/H_2,in}$ was set as in Refs. [16,19], while the lower bound of $\dot{V}_{air,in}$ is set in accordance with Cai et al. [96], avoiding a highly oxidizing atmosphere in the air channel and anode compartment by ensuring the molar fraction X_{N_2} to be > 50% (i.e., $\Psi_{air} > 0.4$) locally at each position.

Having established the parameter setting, Fig. 8 exemplarily displays steady-state solutions of the 3D temperature profiles of the ESC and CSC stack solid phases (Fig. 8c and Fig. 8d also include the peripheral insulation layer) at selected operation points of 1.4 V, 1 atm and 850 °C (ESC) or 700 °C (CSC).

Per cell design, these solutions correspond to a single optimized operation point in the ($T_{g,in}$, E_{cell}, p)-parameter space. As can be extracted from Fig. 8, within the stack solid phase, temperature gradients mainly emerge along the axial flow direction with minimal cross-sectional variations and with no internal hot spot (under the present exothermic conditions) occurring.

Fig. 9 depicts bar diagrams, which illustrate the optimized performance data of the ESC-based Mk200-design 150-cell stack at the chosen temperature bounds of $T_{g,in}$ = 800–900 °C, while Fig. 10 displays the optimized performance data of the CSC-design stack at $T_{g,in}$ = 650–750 °C in an equivalent representation.

From Fig. 9b and Fig. 10b, it can be seen that (in direct congruency to the computed single cells' electrical efficiencies plotted in Fig. 5b and

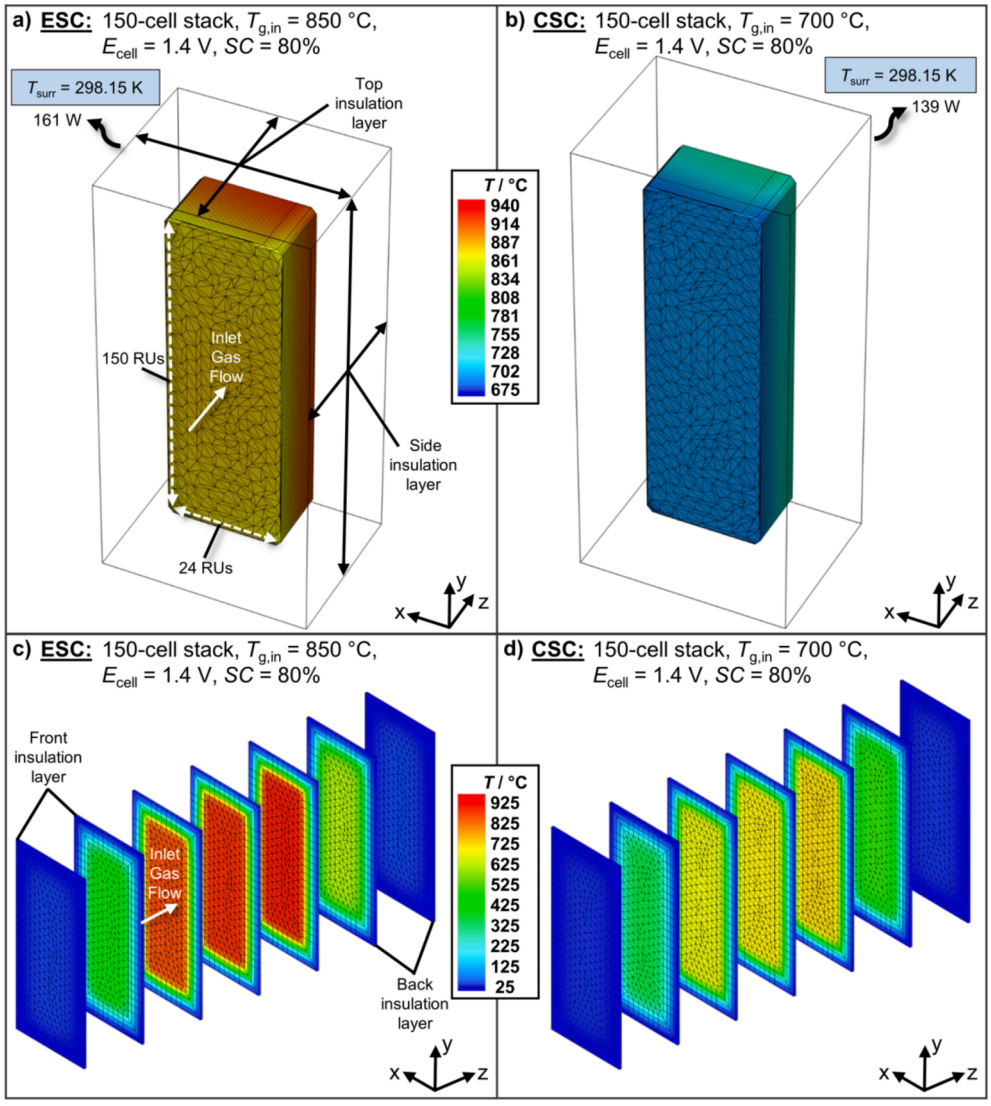

Fig. 8. (a-b) Stack solid phase 3D temperature profiles of Mk200-design 150-cell stacks (peripheral insulation layers indicated with grey contours) operating at E_{cell} = 1.4 V, 90%/10% H_2O/H_2, air, SC = 80%, p = 1 atm, and (c-d) the corresponding axial cut-away views of the 3D temperature profiles including the peripheral insulation layer. Note the two different temperature scales, which are applied for illustrational purposes. The numerical grid is also included in the plots and comprises of triangles discretizing the stack domain, as well as brick elements defining the insulation layer [49]. Heat losses from the insulation boundaries to the surroundings are indicated via curved arrows. (a and c) ESC-based stack, $T_{g,in}$ = 850 °C, (b and d) CSC-based stack, $T_{g,in}$ = 700 °C.

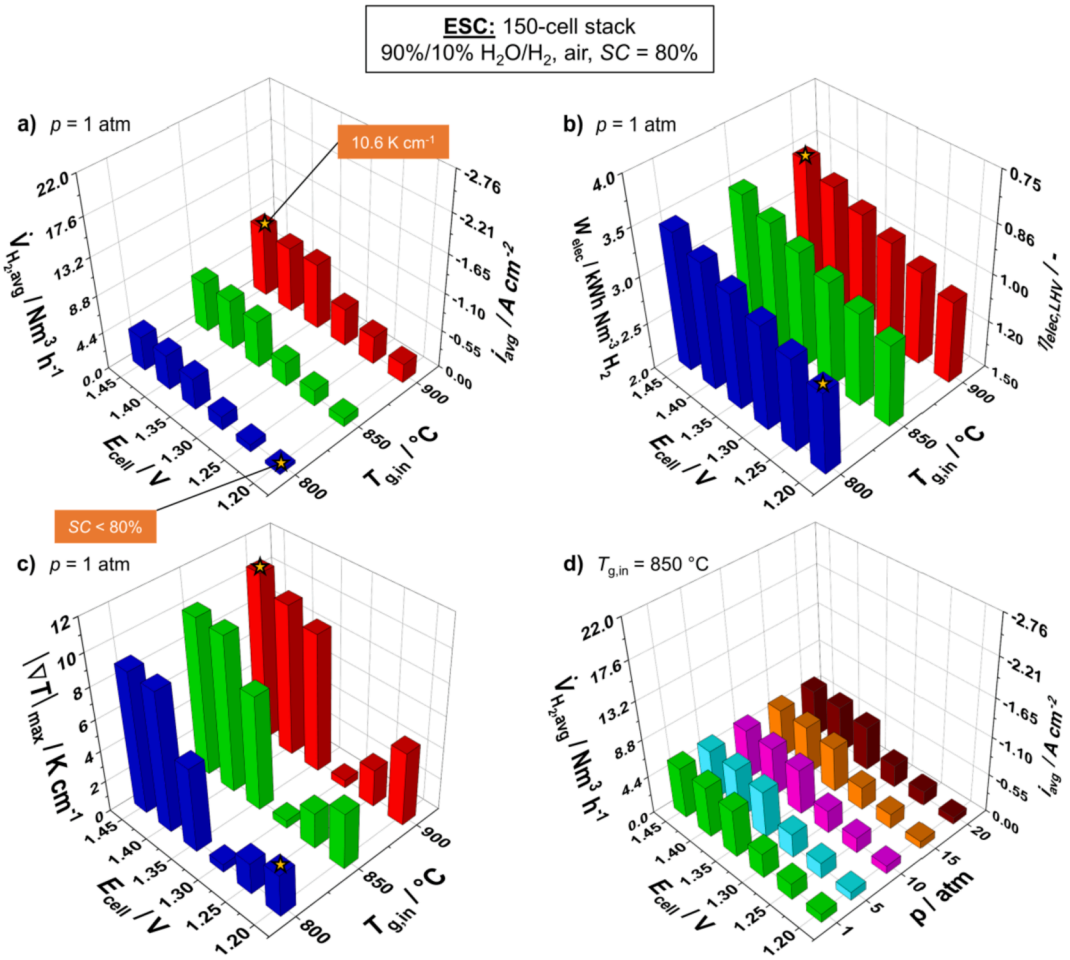

Fig. 9. (a-d) 3D bar diagram depicting the optimized performance of the of the ESC Mk200-design stack in the parameter space spanned by the controllable variables. As described in Section 2.1.3, $\dot{V}_{H_2O/H_2,in}$ and $\dot{V}_{air,in}$ were tuned to maximize $\dot{V}_{H_2,avg}$ and fulfil the optimization constraints defined in Table 7 at each operation point (i.e., colored bar). Operation points marked with a yellow star cannot satisfy at least one of the imposed constraints. Bars correspond to the stack's RU-averaged performance data respectively. Operation conditions: 90%/10% H_2O/H_2, SC = 80%, E_{cell} = 1.2–1.45 V (a-c) $T_{g,in}$ = 800–900 °C, p = 1 atm, d) $T_{g,in}$ = 850 °C, p = 1–20 atm. (For interpretation of the references to colour in this figure legend, the reader is referred to the web version of this article.)

Fig. 6b), the stack's electrical efficiency $\eta_{elec,LHV}$, (or rather W_{elec}, its specific direct current (DC) electric energy demand per Nm^3 of produced H_2, with LHV_{H_2} corresponding to 3.00 kWh Nm^{-3} H_2) is independent of $T_{g,in}$ and a linear function of E_{cell} spanning from ~2.87 kWh Nm^{-3} H_2 ($\eta_{elec,LHV}$ ~ 104%) to ~3.47 kWh Nm^{-3} H_2 ($\eta_{elec,LHV}$ ~ 86%) for E_{cell} = 1.2–1.45 V. This is a direct consequence of the current being proportional to the H_2 production rate, Eq. (4). As depicted in Fig. 9a and Fig. 10a, however, the maximum RU-averaged H_2-production rate $\dot{V}_{H_2,avg}$ that can be reached at each operation point is a strong non-linear function of both E_{cell} and $T_{g,in}$. Aside from the non-linear B-V kinetics, this effect is crucially governed by the stack-internal temperature development (simulated average stack solid-phase temperatures $T_{stack,s,avg}$ are provided in Table S4 and Table S5 for both cell-stacks, respectively). As can be extracted from Fig. 9a and Fig. 10a for both stacks, large $\dot{V}_{H_2,avg}$ increases are possible when enhancing E_{cell} from nearly thermoneutral conditions at 1.3 V to exothermal conditions at 1.35 V (up to a factor of ~2.7 at $T_{g,in}$ = 650 °C for the CSC stack). The benefits of further voltage increments are clearly less pronounced or even vanish entirely, since at the highest E_{cell} of 1.4–1.45 V, large air flow rates are required to limit the rise of the stack solid-phase temperature $T_{stack,s}$ due to the $|\nabla T|_{max}$ constraint that needs to be satisfied. As indicated in Fig. 9a for the ESC stack, with $|\nabla T|_{max}$ approaching the upper limit of 10 K cm^{-1} at 800–850 °C and 1.45 V, the control target is overshot for operation at $T_{g,in}$ = 900 °C, $|\nabla T|_{max}$ = 10.6 K cm^{-1}, even when operating at the upper bound of $\dot{V}_{air,in} = 6 \times \dot{V}_{H_2O/H_2,in}$. As depicted in Fig. 10a for the CSC-design, operation of the stack at 1.45 V at either point within the temperature bounds necessarily exceeds the thermal control target, indicating that a large air flow rate of $> 6 \times \dot{V}_{H_2O/H_2,in}$ would be required to practically operate the stack under these strongly exothermic conditions.

In contrast to the exothermic regime, operation at or close to the lower bound of E_{cell}, i.e. at 1.2 V and 1.25 V, would have the essential benefits of (i) a decreased electricity consumption W_{elec} of the stack (Fig. 9b and 10b) and (ii) reduced electrode overpotentials. Crucially, the cathode overpotential has been identified to play a key role with respect to the long-term stability of the susceptible Ni-based cermet cathodes, initiating irreversible microstructural changes of the percolating Ni network [1,21,23]. Hence, operation at low E_{cell} is a very impactful measure to prevent an onset of cell degradation during continuous steam electrolysis operation. However, the model predicts significant temperature drops during both ESC and CSC stack operation in endothermic mode. Most notably, for the ESC stack in Fig. 9a, considering the lower bounds of E_{cell} at 1.2 V and of $T_{g,in}$ at 800 °C, a significant temperature decline of ΔT ~ -95–100 °C along the axial flow direction with no internal cold spot occurring (comparing $T_{stack,s,avg}$ to $T_{g,in}$, see Table S4) is predicted by the model even after counterbalancing the cooling effect by feeding excess air up to the upper limit, which is now at a higher temperature compared to the gas flow cooling off within

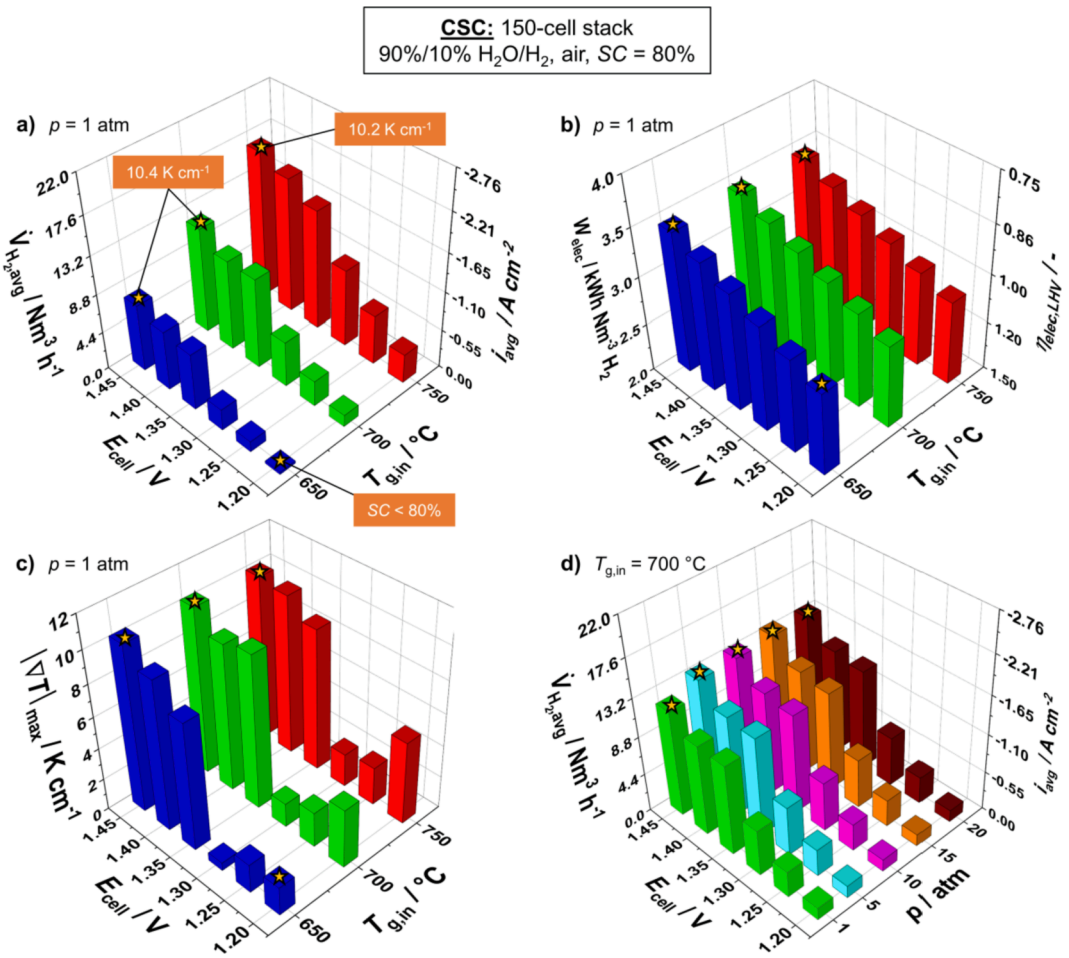

Fig. 10. (a-d) 3D bar diagram depicting the optimized performance of the of the CSC Mk200-design stack in the parameter space spanned by the controllable variables. As described in Section 2.1.3, $\dot{V}_{H_2O/H_2,in}$ and $\dot{V}_{air,in}$ were tuned to maximize $\dot{V}_{H_2,avg}$ and fulfil the optimization constraints defined in Table 7 at each operation point (i.e., colored bar). Operation points marked with a yellow star cannot satisfy at least one of the imposed constraints. Bars correspond to the stack's RU-averaged performance data respectively. Operation conditions: 90%/10% H_2O/H_2, $SC = 80\%$, $E_{cell} = 1.2$–1.45 V (a-c) $T_{g,in} = 650$–750 °C, $p = 1$ atm, d) $T_{g,in} = 700$ °C, $p = 1$–20 atm. (For interpretation of the references to colour in this figure legend, the reader is referred to the web version of this article.)

the stack. For the same reasons, at 1.2 V, the ESC stack can only reach a maximum SC of ~72% at $T_{g,in} = 800$ °C, and the CSC stack only reaches $SC \sim 71\%$ at $T_{g,in} = 650$ °C, which does not satisfy the operation specification of 80%. Under these conditions, the applied cathode/anode flow ratio and the flow-dependent temperature decrease simply cause the stack to be unable to convert the required amount of steam. These results emphasize that at 150-cell stack level due to the large thermal mass of the stack, operation below the TNV to decrease W_{elec} and limit electrode overpotentials is hindered by the fact that operation at large excess air ratios Ψ_{air} would be required to keep the stack at temperature, thereby augmenting the air blower/compressor costs.

The imposed auxiliary costs due to the air compression requirements might be particularly severe under pressurized conditions in the PtM-system. To quantitatively assess the effect of air compression, the BoP compressor power $P_{BoP,\,air}$ was calculated at each operation point for both stacks considering multi-stage adiabatic compression with inter-stage cooling as in Wang et al. [97] by tolerating a maximum pressure ratio of 5 [97], whilst assuming an isentropic compressor efficiency of 85% [98], an adiabatic index of 1.4 [97], and an inter-stage cooling temperature of 40 °C [16]. Lower $P_{BoP,\,air}$ could be possible when adding an air-side recirculation loop to the system layout [28]. However, the implementation of such a loop necessarily enhances system complexity and costs, due to the additional high-pressure high-temperature equipment required (such as pipes, valves, and controllers). It is therefore not considered in this evaluation. The resultant $P_{BoP,\,air}$ with respect to the stack's electric DC input P_{elec} are listed in Tables S4 and S5 respectively. It can be distinguished that at atmospheric pressure, $P_{BoP,\,air}/P_{elec}$ is generally < 1%, while the required compressor power strongly increases during pressurized operation, so that $P_{BoP,\,air}$ can be expected to become a significant contributor to the net system's energy demand. For the ESC-design stack, only the operation points at 1.3–1.35 V and 850–900 °C would enable $P_{BoP,\,air}/P_{elec}$ to be < 10% (provided that considerable performance losses at 1.3 V are tolerated, since for this E_{cell}, the operating conditions minimizing $P_{BoP,\,air}$ are lower than the $\dot{V}_{H_2,avg}$-optimized performance data, note values in square brackets and the footnote in Table S4). Notably, in contrast to the ESC-design stack, the operation points at $E_{cell} = 1.3$ V maximizing $\dot{V}_{H_2,avg}$ also correspond to the conditions minimizing $P_{BoP,\,air}/P_{elec}$ for the CSC stack, i.e., they represent operation at the lower bound of $\dot{V}_{air,in}$. This is because for the CSC-design stack, the heat development due to the increased cell activity ($\dot{Q}_i$ term in Table S1) is sufficient to overcompensate the heat losses. This leads to a net temperature increase, which gets augmented at lower air inlet flow rates. Thus, the CSC-design stack can be operated over the entire temperature range of $T_{g,in} = 650$–750 °C satisfying $P_{BoP,\,air}/P_{elec} \leq 10\%$ at 1.3–1.35 V for $p = 10$ atm, and at 1.3 V for $p = 20$ atm. These considerations clearly suggest that to cost-effectively operate the SOEC stacks under pressurized conditions, feasible operation points only range from thermoneutral to moderately exothermic (1.3–1.35 V) conditions in order to limit the required sweep gas flow rates, since from Tables S4

and S5, it can be distinguished that the efficiency gains at lower E_{cell} would be thoroughly consumed by the sweep gas compression, alongside the additional electrical heating requirements of the inlet streams during endothermic operation further decreasing the system efficiency [19]. A closer heat integration of the PtM plant's SOEC unit with an additional industrial waste heat source at an appropriate temperature level when available [99] could in principle counteract the input electrical power requirements for the heat exchangers under endothermic conditions (but not the higher $P_{BoP,\,air}$). Still, in any case, considerably higher stack and system CAPEX would be resultant, since as this analysis reveals, significantly lower stack power outputs compared to thermoneutral or exothermic conditions are produced even at high $\dot{V}_{air,in}$.

Operation points up to 1.4 V, which also cause higher $P_{BoP,\,air}$ demands compared to less exothermic conditions but stay within the operation constraints specified in Table 7 could be tolerated to maximize $\dot{V}_{H_2,avg}$, e.g. when there temporarily exists surplus electricity or system-specific higher load demands; preferentially when the stack operates at or close to atmospheric pressure. At cell voltages higher than 1.4 V though, there exists a pronounced risk that significant temperature gradients in the axial flow direction (cf. Fig. 8) are occurring during stack operation that might lead to severe thermal stresses in the ceramic components.

Thus, under optimized conditions, the ESC-design stack reaches a maximum of 8.8 kW_{elec} (2.83 $Nm^3\ h^{-1}$) at 1.3 V and 17.7 kW_{elec} (5.51 $Nm^3\ h^{-1}$) at 1.35 V at 850 °C and 1 atm, with slight performance decreases under pressurized conditions, as in case of the single cell studies in Section 3.2. For the CSC-design, it can be deduced from Fig. 10d that the cell-level performance enhancements under pressure (Section 3.2) translate to the stack-scale in such a way that $\dot{V}_{H_2,avg}$ increases of ~5–15% for $T_{g,in}$ = 650–750 °C at p = 5–20 atm compared to operation at atmospheric pressure can be achieved. A direct comparison of the optimized stack performances between both cell designs is provided in Table 8.

At 700 °C and 20 atm, the 150-cell Mk200-design CSC-based stack reaches 17.6 kW_{elec} under thermoneutral (1.3 V) and 36.6 kW_{elec} under moderately exothermic (1.35 V) conditions, whilst ensuring reasonably low air cooling requirements of < 30 sccm cm^{-2} and temperature gradients of < 10 K cm^{-1}. Thus, the simulations predict an approximately doubled power capacity of the CSC stack compared to the ESC design, while operating at a 150 °C reduced temperature. These factors provide a very promising perspective to boost the competitiveness of future SOEC-based PtM-systems for energy storage applications.

It should be clearly emphasized, however, that the electrochemical performance is only one of several important factors for SOEC cell and stack design considerations in PtM-systems. Other aspects like mechanical robustness, flexibility, redox stability and degradation/long-term stability of the selected cell design are also essential factors for successful implementation in PtM-systems, and to realize competitive techno-economic scenarios [1,41]. Still, considering the mechanical stability of the CSC design, state-of-the-art electrode supported cells incorporated in stacks have experimentally demonstrated to successfully withstand severely transient thermal conditions [100] and pressurized operation up to 25 bar [101], thus proving a high level of robustness [1]. While stable performance under dynamic operation has also been successfully demonstrated on stack level with both ESC and CSC types [102,103], the degradation of the Ni-cermet electrode in the CSC design under continuous electrolysis operation remains the critical factor [1]. Here, microstructural optimization is the key to fundamentally improve the electrode's long-term-stability [23,24], and recently, encouraging durability results on stack level with a CSC as considered in this study were published with an observed low voltage degradation of 0.2%/1000 h at 700 °C, 1 atm, and ~1.32 V during the final ~700 h for 1000 h of testing [104]. Though the initial deactivation period [104] should be decreased in future via structural optimization, these results support the fact that such high-performance cell designs could indeed be successfully integrated in upcoming PtM-systems.

Moreover, it should be noted that while this study specifically focuses on performance benchmarking SOEC stacks for PtM-systems via the selected optimization bounds, operation specifications and constraints, these are also applicable up to a certain level to other Power-to-X concepts thermally integrating an SOEC unit performing steam electrolysis (i.e., not co-electrolysis as another possible concept [105]) with downstream chemical synthesis reactors, such as Power-to-Ammonia [106] and Power-to-Methanol [105]. However, most notably, different pressure levels of the electrolyzer might be favorable and different requirements of the steam conversion level in the SOEC cathode stream might exist as a result of varying chemical reactor systems and individual plant concepts.

4. Conclusions

A combined experimental and detailed modelling methodology was used to benchmark the SOEC steam electrolysis performance of commercial Ni-CGO/LSCF electrolyte-supported and Ni-YSZ/LSC cathode-supported cell designs for Power-to-Methane applications. While the primary purpose of the work was to optimize the cells' operating conditions on 150-cell industrial-scale stack level, and to evaluate the impact of different cell configurations on the stack performance by using a detailed multi-scale model, the study also details the model's parametrization, validation and scale-up procedure.

In a first step, the microstructure of each cell type was analyzed to parametrize a 2D adiabatic single cell model, which then in turn was comprehensively calibrated and validated based on the recorded polarization and impedance data (700–900 °C for ESC, 600–750 °C for CSC, both at 90%/10% H_2O/H_2, air). For both cell types, the model showed a very good accordance with the experimental data across a broad temperature and polarization range. Additionally, literature data was considered for validating the model under pressurized conditions, and particular care was taken for all datasets in order not to over-fit the experiments with respect to the kinetic or microstructural parameters.

Subsequently, the as-calibrated model was used to map the performances of both cell types at E_{cell} = 1.2–1.45 V, SC = 25–100%, p = 1–20 atm and temperature ranges of 750–850 °C (ESC) or 650–750 °C (CSC). It was found that in contrast to the cell's electrical efficiency $\eta_{elec,LHV}$, which is not a function of the steam conversion SC at constant cell voltage, the efficiency based on the total (heat plus electrical) energy input η_{LHV} is, however, dependent on SC. The singe-cell simulations revealed that there exists a cell-specific threshold steam conversion of ~80% for the ESC and ~75% for the CSC design, which, individually, represent maximum η_{LHV} due to the impact of reactant starvation zones on the cell performance. Since the threshold SC was found to be

Table 8
Stack performance data of Mk200-design ESC- and CSC-based 150-cell stacks at optimized, system-oriented operation points.

Performance metric	@Cell voltage	ESC: 850 °C			CSC: 700 °C		
		1 atm	10 atm	20 atm	1 atm	10 atm	20 atm
$\dot{V}_{H_2,avg}$/ $Nm^3\ h^{-1}$	1.3 V	2.83	2.63	2.58	5.26	5.65	5.64
	1.35 V	5.51	5.27	5.14	10.4	11.3	11.5
P_{elec}/ kW	1.3 V	8.8	8.2	8.0	16.4	17.6	17.6
	1.35 V	17.8	17.0	16.6	33.4	36.6	36.6

independent of the cell voltage, temperature and pressure, it can be used to appraise when reactant shortage within the cell could cause net efficiency losses at the PtM system scale. Moreover, in line with experimental results [41], the model predicts reduced cell-level performance in case of the ESC at elevated pressures as compared to atmospheric pressure (~-9% at 1.35 V,SC = 80%, 20 atm, 850 °C) due to the large R_{ohm}, while predicting performance gains for the CSC (~+9% at 1.35 V, SC = 80%, 20 atm, 700 °C). This showcases specific advantages of the CSC design for PtM-applications when pressurized operation conditions are considered to facilitate plant integration [9,10]. Afterwards, the hierarchical modeling approach was used to move up in scale reaching the industrial-sized stack level. For the two stack designs individually, optimization studies with the full 3D-model were conducted in broad parameter spaces. Accounting for practical stack operation constraints and operation specifications, which are a result of the PtM-system demands, stack performances under application-oriented conditions were assessed. From these studies, the following conclusions can be drawn:

- At the commercial-scale stack level for both stack designs, operation below the TNV at $\leq$ 1.25 V is severely limited (i) by the temperature drop (up to 74 °C at 1.2 V even at $\dot{V}_{air,in} = 6 \times \dot{V}_{H_2O/H_2,in}$) irrespective of the absolute pressure due to the large thermal mass of the stack and (ii) by the parasitic sweep gas compression costs during pressurized operation conditions due to the high flow rate required to limit the temperature drop.
- Operation under high load conditions, i.e., at cell voltages $\geq$ 1.4 V, is also limited for both stack designs (i) due to the required sweep gas flow rate under pressurized operation conditions to limit the temperature rise and (ii) due to the steady-state temperature gradient itself. When permitting a higher $|\nabla T|_{max}$, i.e., using very thermo-mechanically robust stack designs as e.g. tested by Hagen et al. [100], operation at these voltages might be tolerated at the expense of the SOEC unit's efficiency to temporarily maximize the H_2 production rate when there exist system-specific higher load demands or surplus energy.

These outcomes are largely influenced by the stack's large thermal mass, so that the importance of detailed stack-modeling approaches to predict the temperature development in kW-class stacks can be plainly seen.

Under optimized and application-oriented conditions (1.3–1.35 V, SC = 80%, 1–20 atm) the model results suggest the Mk200-design CSC-based stack to reach a ~2 times higher H_2 output rate at $T_{g,in}$ = 700 °C compared to the ESC-based stack operating at $T_{g,in}$ = 850 °C. Thus, for the CSC-design at 1.35 V, a remarkable stack capacity P_{elec} of up to 36.6 kW at 1.35 V is predicted whilst ensuring safe temperature gradients.

As part of future work, the as-developed stack simulation tool will be incorporated into fully integrated SOEC-based PtM process models to optimize the conceptual design of various PtM-layouts involving different catalytic methanation concepts and CO_2 sources.

CRediT authorship contribution statement

Lukas Wehrle: Conceptualization, Methodology, Software, Investigation, Writing – original draft. **Daniel Schmider:** Validation, Investigation, Writing – original draft. **Julian Dailly:** Conceptualization, Methodology, Validation, Investigation, Writing – review & editing, Supervision, Funding acquisition. **Aayan Banerjee:** Conceptualization, Methodology, Software, Writing – review & editing. **Olaf Deutschmann:** Conceptualization, Writing – review & editing, Supervision, Funding acquisition.

Declaration of Competing Interest

The authors declare that they have no known competing financial interests or personal relationships that could have appeared to influence the work reported in this paper.

Acknowledgements

The Steinbeis GmbH für Technologietransfer (STZ 240 Reaktive Strömung) is gratefully acknowledged for a cost-free academic license of DETCHEM™.

Financial support by the German federal ministry for economic affairs and energy (Bundesministerium für Wirtschaft und Energie, BMWi) under Grant Numbers 03EIV041D and 03EIV041E in the "MethFuel" group of the collaborative research project "MethQuest" is gratefully acknowledged.

Lukas Wehrle would also like to thank Dr. Yuqing Wang from Beijing Institute of Technology for the very insightful discussions during the course of this work.

Appendix A. Supplementary data

Supplementary data to this article can be found online at https://doi.org/10.1016/j.apenergy.2022.119143.

References

[1] Hauch A, Küngas R, Blennow P, Hansen AB, Hansen JB, Mathiesen BV et al. Recent advances in solid oxide cell technology for electrolysis. Science 2020;370 (6513):eaba6118. 10.1126/science.aba6118.
[2] Wulf C, Linssen J, Zapp P. Power-to-Gas—Concepts, Demonstration, and Prospects. In: Azzaro-Pantel C, editor. Hydrogen Supply Chains - Design, Deployment and Operation, London: Elsevier; 2018, p. 309–345. 10.1016/B978-0-12-811197-0.00009-9.
[3] Götz M, Lefebvre J, Mörs F, McDaniel Koch A, Graf F, Bajohr S, et al. Renewable Power-to-Gas: A technological and economic review. Renewable Energy 2016;85: 1371–90.
[4] Iskov H, Rasmussen NB. Global screening of projects and technologies for Power-to-Gas and Bio-SNG. Hørsholm: A reference report. Danish Gas Technology Centre; 2013.
[5] Thema M, Bauer F, Sterner M. Power-to-Gas: Electrolysis and methanation status review. Renewable Sustainable Energy Rev 2019;112:775–87. https://doi.org/10.1016/j.rser.2019.06.030.
[6] Peters R, Deja R, Blum L, van Nguyen N, Fang Q, Stolten D. Influence of operating parameters on overall system efficiencies using solid oxide electrolysis technology. Int J Hydrogen Energy 2015;40(22):7103–13. https://doi.org/10.1016/j.ijhydene.2015.04.011.
[7] Brisse A, Schefold J, Zahid M. High temperature water electrolysis in solid oxide cells. Int J Hydrogen Energy 2008;33(20):5375–82. https://doi.org/10.1016/j.ijhydene.2008.07.120.
[8] Laguna-Bercero MA. Recent advances in high temperature electrolysis using solid oxide fuel cells: A review. J Power Sources 2012;203:4–16. https://doi.org/10.1016/j.jpowsour.2011.12.019.
[9] Gruber M, Weinbrecht P, Biffar L, Harth S, Trimis D, Brabandt J, et al. Power-to-Gas through thermal integration of high-temperature steam electrolysis and carbon dioxide methanation - Experimental results. Fuel Process Technol 2018; 181:61–74.
[10] Anghilante R, Müller C, Schmid M, Colomar D, Ortloff F, Spörl R, et al. Innovative power-to-gas plant concepts for upgrading of gasification bio-syngas through steam electrolysis and catalytic methanation. Energy Convers Manage 2019;183: 462–73.
[11] Brabandt J, Posdziech O. System Approach of a Pressurized High-Temperature Electrolysis. ECS Trans 2017;78(1):2987–95. https://doi.org/10.1149/07801.2987ecst.
[12] Lehner M, Tichler R, Steinmüller H, Koppe M. Power-to-Gas: Technology and Business Models, Cham: Springer; 2014. 10.1007/978-3-319-03995-4.
[13] Engerer H, Horn M. Natural gas vehicles: An option for Europe. Energy Policy 2010;38(2):1017–29. https://doi.org/10.1016/j.enpol.2009.10.054.
[14] Posdziech O, Geißler T, Schwarze K, Blumentritt R. System Development and Demonstration of Large-Scale High-Temperature Electrolysis. ECS Trans 2019;91 (1):2537–46. https://doi.org/10.1149/09101.2537ecst.
[15] Banerjee A, Wang Y, Diercks J, Deutschmann O. Hierarchical modeling of solid oxide cells and stacks producing syngas via H_2O/CO_2 Co-electrolysis for industrial applications. Appl Energy 2018;230:996–1013. https://doi.org/10.1016/j.apenergy.2018.08.122.
[16] Wang L, Rao M, Diethelm S, Lin T-E, Zhang H, Hagen A, et al. Power-to-methane via co-electrolysis of H_2O and CO_2: The effects of pressurized operation and internal methanation. Appl Energy 2019;250:1432–45.
[17] Giglio E, Deorsola FA, Gruber M, Harth SR, Morosanu EA, Trimis D, et al. Power-to-Gas through High Temperature Electrolysis and Carbon Dioxide Methanation: Reactor Design and Process Modeling. Ind Eng Chem Res 2018;57(11):4007–18.

[18] Wang L, Düll J, Maréchal F, van herle J. Trade-off designs and comparative exergy evaluation of solid-oxide electrolyzer based power-to-methane plants. Int J Hydrogen Energy 2019;44(19):9529–43. 10.1016/j.ijhydene.2018.11.151.

[19] Wang L, Pérez-Fortes M, Madi H, Diethelm S, herle JV, Maréchal F. Optimal design of solid-oxide electrolyzer based power-to-methane systems: A comprehensive comparison between steam electrolysis and co-electrolysis. Appl Energy 2018;211:1060–79.

[20] ETOGAS GmbH, Industriestraße 6, GER-70565 Stuttgart. Power-To-Gas-Anlage Bau und Betrieb einer 6-MW-Anlage in Werlte. https://docplayer.org/52818360-Etogas-gmbh-stephan-rieke-power-to-gas-anlage-bau-und-betrieb-einer-6-mw-anlage-in-werlte-muenchen-industriestrasse-6-d-stuttgart.html; 2016 [accessed November 2021].

[21] Schefold J, Brisse A, Poepke H. 23,000 h steam electrolysis with an electrolyte supported solid oxide cell. Int J Hydrogen Energy 2017;42(19):13415–26. https://doi.org/10.1016/j.ijhydene.2017.01.072.

[22] Schefold J, Brisse A, Surrey A, Walter C. 80,000 current on/off cycles in a one year long steam electrolysis test with a solid oxide cell. Int J Hydrogen Energy 2020;45(8):5143–54. https://doi.org/10.1016/j.ijhydene.2019.05.124.

[23] Hauch A, Brodersen K, Chen M, Mogensen MB. Ni/YSZ electrodes structures optimized for increased electrolysis performance and durability. Solid State Ionics 2016;293:27–36. https://doi.org/10.1016/j.ssi.2016.06.003.

[24] Chen M, Tong X, Ovtar S. Lessons Learned from Operating a Solid Oxide Electrolysis Cell at 1.25 a/cm^2 for One Year. ECS Trans 2021;103(1):475–86. https://doi.org/10.1149/10301.0475ecst.

[25] Sunfire GmbH, Gasanstaltstraße 2, GER-01237 Dresden. GrInHy 2.0 project. https://www.green-industrial-hydrogen.com/; 2021 [accessed November 2021].

[26] Salomone F, Giglio E, Ferrero D, Santarelli M, Pirone R, Bensaid S. Techno-economic modelling of a Power-to-Gas system based on SOEC electrolysis and CO_2 methanation in a RES-based electric grid. Chem Eng J 2019;377:120233. https://doi.org/10.1016/j.cej.2018.10.170.

[27] Collet P, Flottes E, Favre A, Raynal L, Pierre H, Capela S, et al. Techno-economic and Life Cycle Assessment of methane production via biogas upgrading and power to gas technology. Appl Energy 2017;192:282–95.

[28] Jeanmonod G, Wang L, Diethelm S, Maréchal F, van herle J. Trade-off designs of power-to-methane systems via solid-oxide electrolyzer and the application to biogas upgrading. Appl Energy 2019;247:572–81. https://doi.org/10.1016/j.apenergy.2019.04.055.

[29] Bernadet L, Gousseau G, Chatroux A, Laurencin J, Mauvy F, Reytier M. Influence of pressure on solid oxide electrolysis cells investigated by experimental and modeling approach. Int J Hydrogen Energy 2015;40(38):12918–28. https://doi.org/10.1016/j.ijhydene.2015.07.099.

[30] Bernadet L, Laurencin J, Roux G, Montinaro D, Mauvy F, Reytier M. Effects of Pressure on High Temperature Steam and Carbon Dioxide Co-electrolysis. Electrochim Acta 2017;253:114–27. https://doi.org/10.1016/j.electacta.2017.09.037.

[31] Aicart J, Petitjean M, Laurencin J, Tallobre L, Dessemond L. Accurate predictions of H_2O and CO_2 co-electrolysis outlet compositions in operation. Int J Hydrogen Energy 2015;40(8):3134–48. https://doi.org/10.1016/j.ijhydene.2015.01.031.

[32] Chatzichristodoulou C, Chen M, Hendriksen PV, Jacobsen T, Mogensen MB. Understanding degradation of solid oxide electrolysis cells through modeling of electrochemical potential profiles. Electrochim Acta 2016;189:265–82. https://doi.org/10.1016/j.electacta.2015.12.067.

[33] Ni M. 2D thermal modeling of a solid oxide electrolyzer cell (SOEC) for syngas production by H_2O/CO_2 co-electrolysis. Int J Hydrogen Energy 2012;37(8):6389–99. https://doi.org/10.1016/j.ijhydene.2012.01.072.

[34] Al-Masri A, Peksen M, Blum L, Stolten D. A 3D CFD model for predicting the temperature distribution in a full scale APU SOFC short stack under transient operating conditions. Appl Energy 2014;135:539–47. https://doi.org/10.1016/j.apenergy.2014.08.052.

[35] Li A, Song C, Lin Z. A multiphysics fully coupled modeling tool for the design and operation analysis of planar solid oxide fuel cell stacks. Appl Energy 2017;190:1234–44. https://doi.org/10.1016/j.apenergy.2017.01.034.

[36] Navasa M, Miao X-Y, Frandsen HL. A fully-homogenized multiphysics model for a reversible solid oxide cell stack. Int J Hydrogen Energy 2019;44(41):23330–47. https://doi.org/10.1016/j.ijhydene.2019.06.077.

[37] Lin C-K, Chen T-T, Chyou Y-P, Chiang L-K. Thermal stress analysis of a planar SOFC stack. J Power Sources 2007;164(1):238–51. https://doi.org/10.1016/j.jpowsour.2006.10.089.

[38] Zheng Y, Wang J, Yu Bo, Zhang W, Chen J, Qiao J, et al. A review of high temperature co-electrolysis of H_2O and CO_2 to produce sustainable fuels using solid oxide electrolysis cells (SOECs): advanced materials and technology. Chem Soc Rev 2017;46(5):1427–63.

[39] Udomsilp D, Lenser C, Guillon O, Menzler NH. Performance Benchmark of Planar Solid Oxide Cells Based on Material Development and Designs. Energy Technol 2021;9(4):2001062. https://doi.org/10.1002/ente.202001062.

[40] Ye L, Xie K. High-temperature electrocatalysis and key materials in solid oxide electrolysis cells. J Energy Chem 2021;54:736–45. https://doi.org/10.1016/j.jechem.2020.06.050.

[41] Riedel M, Heddrich MP, Ansar A, Fang Q, Blum L, Friedrich KA. Pressurized operation of solid oxide electrolysis stacks: An experimental comparison of the performance of 10-layer stacks with fuel electrode and electrolyte supported cell concepts. J Power Sources 2020;475:228682. https://doi.org/10.1016/j.jpowsour.2020.228682.

[42] Yan Y, Fang Q, Blum L, Lehnert W. Performance and degradation of an SOEC stack with different cell components. Electrochim Acta 2017;258:1254–61. https://doi.org/10.1016/j.electacta.2017.11.180.

[43] Preininger M, Stoeckl B, Subotić V, Hochenauer C. Characterization and performance study of commercially available solid oxide cell stacks for an autonomous system. Energy Convers Manage 2020;203:112215. https://doi.org/10.1016/j.enconman.2019.112215.

[44] Menon V, Fu Q, Janardhanan VM, Deutschmann O. A model-based understanding of solid-oxide electrolysis cells (SOECs) for syngas production by H_2O/CO_2 co-electrolysis. J Power Sources 2015;274:768–81. https://doi.org/10.1016/j.jpowsour.2014.09.158.

[45] Zhu H, Kee RJ, Janardhanan VM, Deutschmann O, Goodwin DG. Modeling Elementary Heterogeneous Chemistry and Electrochemistry in Solid-Oxide Fuel Cells. J Electrochem Soc 2005;152(12). https://doi.org/10.1149/1.2116607.

[46] Bessler WG, Gewies S. Gas Concentration Impedance of Solid Oxide Fuel Cell Anodes. J Electrochem Soc 2007;154(6). https://doi.org/10.1149/1.2720639.

[47] Donazzi A, de Pascali S, Garavaglia F, Bracconi M. A quasi 2D model for the interpretation of impedance and polarization of a planar solid oxide fuel cell with interconnects. Electrochim Acta 2021;365:137346. https://doi.org/10.1016/j.electacta.2020.137346.

[48] Costamagna P, Honegger K. Modeling of Solid Oxide Heat Exchanger Integrated Stacks and Simulation at High Fuel Utilization. J Electrochem Soc 1998;145(11):3995–4007. https://doi.org/10.1149/1.1838904.

[49] Tischer S, Deutschmann O. Recent advances in numerical modeling of catalytic monolith reactors. Catal Today 2005;105(3–4):407–13. https://doi.org/10.1016/j.cattod.2005.06.061.

[50] Liu S, Song C, Lin Z. The effects of the interconnect rib contact resistance on the performance of planar solid oxide fuel cell stack and the rib design optimization. J Power Sources 2008;183(1):214–25. https://doi.org/10.1016/j.jpowsour.2008.04.054.

[51] Deutschmann O, Tischer S, Correa C, Chatterjee D, Kleditzsch S, Janarhanan VM, Mladenov N, Minh HD, Karadeniz H, Hettel M, Menon V, Banerjee A, Goßler H. DETCHEM^{TM}, www.detchem.com, Karlsruhe; 2020.

[52] Deuflhard P, Hairer E, Zugck J. One-step and extrapolation methods for differential-algebraic systems. Numer Math 1987;51(5):501–16. https://doi.org/10.1007/BF01400352.

[53] Janardhanan VM, Deutschmann O. Numerical study of mass and heat transport in solid-oxide fuel cells running on humidified methane. Chem Eng Sci 2007;62(18–20):5473–86. https://doi.org/10.1016/j.ces.2007.01.043.

[54] Gossler H, Maier L, Angeli S, Tischer S, Deutschmann O. CaRMeN: a tool for analysing and deriving kinetics in the real world. Phys Chem Chem Phys 2018;20(16):10857–76. https://doi.org/10.1039/C7CP07777G.

[55] Gao Z, Mogni LV, Miller EC, Railsback JG, Barnett SA. A perspective on low-temperature solid oxide fuel cells. Energy Environ Sci 2016;9(5):1602–44. https://doi.org/10.1039/c5ee03858h.

[56] Nam JH, Jeon DH. A comprehensive micro-scale model for transport and reaction in intermediate temperature solid oxide fuel cells. Electrochim Acta 2006;51(17):3446–60. https://doi.org/10.1016/j.electacta.2005.09.041.

[57] Bertei A, Nicolella C. A comparative study and an extended theory of percolation for random packings of rigid spheres. Powder Technol 2011;213(1–3):100–8. https://doi.org/10.1016/j.powtec.2011.07.011.

[58] Bertei A, Nicolella C. Percolation theory in SOFC composite electrodes: Effects of porosity and particle size distribution on effective properties. J Power Sources 2011;196(22):9429–36. https://doi.org/10.1016/j.jpowsour.2011.06.087.

[59] Lanfrey P-Y, Kuzeljevic ZV, Dudukovic MP. Tortuosity model for fixed beds randomly packed with identical particles. Chem Eng Sci 2010;65(5):1891–6. https://doi.org/10.1016/j.ces.2009.11.011.

[60] Janardhanan VM, Deutschmann O. Modeling diffusion limitation in solid-oxide fuel cells. Electrochim Acta 2011;56(27):9775–82. https://doi.org/10.1016/j.electacta.2011.08.038.

[61] Suciu C, Tikkanen H, Wærnhus I, Goga F, Dorolti E. Water-based tape-casting of SOFC composite 3YSZ/8YSZ electrolytes and ionic conductivity of their pellets. Ceram Int 2012;38(1):357–65. https://doi.org/10.1016/j.ceramint.2011.07.014.

[62] Ferguson JR, Fiard JM, Herbin R. Three-dimensional numerical simulation for various geometries of solid oxide fuel cells. J Power Sources 1996;58(2):109–22. https://doi.org/10.1016/0378-7753(95)02269-4.

[63] Atkinson A, Baron SA, Brandon NP. AC Impedance Spectra Arising from Mixed Ionic Electronic Solid Electrolytes. J Electrochem Soc 2004;151(5):E186–93. https://doi.org/10.1149/1.1690291.

[64] Steele B. Appraisal of $Ce_{1-y}Gd_yO_{2-y/2}$ electrolytes for IT-SOFC operation at 500°C. Solid State Ionics 2000;129(1–4):95–110. https://doi.org/10.1016/S0167-2738(99)00319-7.

[65] Stevenson JW, Armstrong TR, Carneim RD, Pederson LR, Weber WJ. Electrochemical Properties of Mixed Conducting Perovskites $La_{1-x}M_xCo_{1-y}Fe_yO_{3-\delta}$ (M = Sr, Ba, Ca). J Electrochem Soc 1996;143(9):2722–9. https://doi.org/10.1149/1.1837098.

[66] Fan B, Yan J, Yan X. The ionic conductivity, thermal expansion behavior, and chemical compatibility of $La_{0.54}Sr_{0.44}Co_{0.2}Fe_{0.8}O_{3-\delta}$ as SOFC cathode material. Solid State Sci 2011;13(10):1835–9. https://doi.org/10.1016/j.solidstatesciences.2011.07.007.

[67] Søgaard M, Hendriksen P, Mogensen M, Poulsen F, Skou E. Oxygen nonstoichiometry and transport properties of strontium substituted lanthanum cobaltite. Solid State Ionics 2006;177(37–38):3285–96. https://doi.org/10.1016/j.ssi.2006.09.005.

[68] Teraoka Y, Zhang HM, Okamoto K, Yamazoe N. Mixed ionic-electronic conductivity of $La_{1-x}Sr_xCo_{1-y}Fe_yO_{3-\delta}$ perovskite-type oxides. Mater Res Bull 1988;23(1):51–8. https://doi.org/10.1016/0025-5408(88)90224-3.

[69] Chase, MW. NIST-JANAF Thermochemical Tables, 4th ed. J Phys Chem Ref Data, Monograph 9, New York: American Institute of Physics; 1998.

[70] Jordan L, Swanger WH. The properties of pure Nickel. Bur Standards J Res 1930; 5:1291–307.

[71] Powell RW, Tye RP, Hickman MJ. The thermal conductivity of nickel. Int J Heat Mass Transfer 1965;8(5):679–88. https://doi.org/10.1016/0017-9310(65)90017-7.

[72] Schlichting KW, Padture NP, Klemens PG. J Mater Sci 2001;36(12):3003–10. https://doi.org/10.1023/A:1017970924312.

[73] Radovic M, Lara-Curzio E, Trejo RM, Wang H, Porter WD. Thermophysical Properties of YSZ and Ni-YSZ as a Function of Temperature and Porosity. In: Bansal NP, Wereszczak A, Lara-Curzio E, editors. Advances in Solid Oxide Fuel Cells II: Ceramic Engineering and Science Proceedings, Volume 27, Issue 4. Hoboken, NJ, USA: John Wiley & Sons, Inc; 2006, p. 79–85. 10.1002/9780470291337.ch8.

[74] Reddy KR, Karan K. Sinterability, Mechanical, Microstructural, and Electrical Properties of Gadolinium-Doped Ceria Electrolyte for Low-Temperature Solid Oxide Fuel Cells. J Electroceram 2005;15(1):45–56. https://doi.org/10.1007/s10832-005-1099-4.

[75] Wang C, Tomov RI, Vasant Kumar R, Glowacki BA. Inkjet printing of gadolinium-doped ceria electrolyte on NiO-YSZ substrates for solid oxide fuel cell applications. J Mater Sci 2011;46(21):6889–96. https://doi.org/10.1007/s10853-011-5653-y.

[76] Muthukkumaran K, Kuppusami P, Srinivasan R, Ramachandran K, Mohandas E, Selladurai S. Thermal properties of 15-mol% gadolinia doped ceria thin films prepared by pulsed laser ablation. Ionics 2007;13(1):47–50. https://doi.org/10.1007/s11581-007-0068-0.

[77] Esquirol A, Brandon NP, Kilner JA, Mogensen M. Electrochemical Characterization of $La_{0.6}Sr_{0.4}Co_{0.2}Fe_{0.8}O_3$ Cathodes for Intermediate-Temperature SOFCs. J Electrochem Soc 2004;151(11). https://doi.org/10.1149/1.1799391.

[78] Shin Y-C, Hashimoto S, Yashiro K, Amezawa K, Kawada T. Thermal Properties of Perovskite-Type Oxides $La_{0.6}Sr_{0.4}Co_{1-x}Fe_{x\ O3}.\delta$ ($0 \leq x \leq 1.0$). ECS Trans 2016;72(7):105–10. https://doi.org/10.1149/07207.0105ecst.

[79] Samat AA, Jais AA, Somalu MR, Osman N, Muchtar A, Lim KL. Electrical and electrochemical characteristics of $La_{0.6}Sr_{0.4}CoO_{3-\delta}$ cathode materials synthesized by a modified citrate-EDTA sol-gel method assisted with activated carbon for proton-conducting solid oxide fuel cell application. J Sol-Gel Sci Technol 2018;86(3):617–30. https://doi.org/10.1007/s10971-018-4675-1.

[80] Railsback J, Hughes G, Mogni L, Montenegro-Hernández A, Barnett S. High-Pressure Performance of Mixed-Conducting Oxygen Electrodes: Effect of Interstitial versus Vacancy Conductivity. J Electrochem Soc 2016;163(13). https://doi.org/10.1149/2.1071613jes.

[81] Lu Y, Kreller C, Adler SB. Measurement and Modeling of the Impedance Characteristics of Porous $La_{1-x}Sr_xCoO_{3-\delta}$ Electrodes. J Electrochem Soc 2009;156(4). https://doi.org/10.1149/1.3079337.

[82] Riegraf M, Costa R, Schiller G, Friedrich KA, Dierickx S, Weber A. Electrochemical Impedance Analysis of Symmetrical Ni/Gadolinium-Doped Ceria (CGO10) Electrodes in Electrolyte-Supported Solid Oxide Cells. J Electrochem Soc 2019;166(13):F865–72. https://doi.org/10.1149/2.0051913jes.

[83] Leonide A, Apel Y, Ivers-Tiffee E. SOFC Modeling and Parameter Identification by Means of Impedance Spectroscopy. ECS Trans 2009;19(20):81–109. https://doi.org/10.1149/1.3247567.

[84] Goodwin DG, Zhu H, Colclasure AM, Kee RJ. Modeling Electrochemical Oxidation of Hydrogen on Ni–YSZ Pattern Anodes. J Electrochem Soc 2009;156(9):B1004–21. https://doi.org/10.1149/1.3148331.

[85] Ouyang M, Bertei A, Cooper SJ, Wu Y, Boldrin P, Liu X, et al. Model-guided design of a high performance and durability Ni nanofiber/ceria matrix solid oxide fuel cell electrode. J Energy Chem 2021;56:98–112.

[86] Tsoga A, Naoumidis A, Jungen W, Stöver D. Processing and characterisation of fine crystalline ceria gadolinia–yttria stabilized zirconia powders. J Eur Ceram Soc 1999;19(6–7):907–12. https://doi.org/10.1016/S0955-2219(98)00342-2.

[87] Riedel M, Heddrich MP, Friedrich KA. Analysis of pressurized operation of 10 layer solid oxide electrolysis stacks. Int J Hydrogen Energy 2019;44(10):4570–81. https://doi.org/10.1016/j.ijhydene.2018.12.168.

[88] van Biert L, Godjevac M, Visser K, Aravind PV. Dynamic modelling of a direct internal reforming solid oxide fuel cell stack based on single cell experiments. Appl Energy 2019;250:976–90. https://doi.org/10.1016/j.apenergy.2019.05.053.

[89] Sick K, Grigorev N, Menzler NH, Guillon O. Development of Cathode Contacting for SOFC Stacks. In: Salem J, Koch D, Mechnich P, Kusnezoff M, Bansal N, LaSalvia J et al., editors. Proceeding of the 42nd International Conference on Advanced Ceramics and Composites. Hoboken, NJ, USA: John Wiley & Sons, Inc; 2019, p. 99–111. 10.1002/9781119543343.ch9.

[90] Tallgren J, Himanen O, Bianco M, Mikkola J, Thomann O, Rautanen M, et al. Method to Measure Area Specific Resistance and Chromium Migration Simultaneously from Solid Oxide Fuel Cell Interconnect Materials. Fuel Cells 2019;19(5):570–7.

[91] ThyssenKrupp VDM GmbH, Plettenberger Str. 2, D-58791 Werdohl. Crofer 22 APU technical data sheet.

[92] Green DW, Southard MZ. Perry's Chemical Engineers' Handbook. 9th ed. New York: McGraw-Hill Education; 2019.

[93] Etex Industry c/o Mircotherm N. V., Industriepark-Noord 1, BEL-9100 Sint Niklaas. PROMALIGHT® technical data sheet. https://www.promat-hpi.com; 2021 (accessed November 2021).

[94] Damm DL, Fedorov AG. Spectral Radiative Heat Transfer Analysis of the Planar SOFC. J Fuel Cell Sci Technol 2005;2(4):258–62. https://doi.org/10.1115/1.2041667.

[95] Aguiar P, Adjiman CS, Brandon NP. Anode-supported intermediate-temperature direct internal reforming solid oxide fuel cell. J Power Sources 2005;147(1–2):136–47. https://doi.org/10.1016/j.jpowsour.2005.01.017.

[96] Cai Q, Brandon NP, Adjiman CS. Modelling the dynamic response of a solid oxide steam electrolyser to transient inputs during renewable hydrogen production. Front Energy Power Eng China 2010;4(2):211–22. https://doi.org/10.1007/s11708-010-0037-6.

[97] Wang Y, Banerjee A, Wehrle L, Shi Y, Brandon N, Deutschmann O. Performance analysis of a reversible solid oxide cell system based on multi-scale hierarchical solid oxide cell modelling. Energy Convers Manage 2019;196:484–96. https://doi.org/10.1016/j.enconman.2019.05.099.

[98] Mottaghizadeh P, Santhanam S, Heddrich MP, Friedrich KA, Rinaldi F. Process modeling of a reversible solid oxide cell (r-SOC) energy storage system utilizing commercially available SOC reactor. Energy Convers Manage 2017;142:477–93. https://doi.org/10.1016/j.enconman.2017.03.010.

[99] Papapetrou M, Kosmadakis G, Cipollina A, La Commare U, Micale G. Industrial waste heat: Estimation of the technically available resource in the EU per industrial sector, temperature level and country. Appl Therm Eng 2018;138:207–16. https://doi.org/10.1016/j.applthermaleng.2018.04.043.

[100] Hagen A, Wulff AC, Zielke P, Sun X, Talic B, Ritucci I, et al. SOFC stacks for mobile applications with excellent robustness towards thermal stresses. Int J Hydrogen Energy 2020;45(53):29201–11.

[101] Jensen SH, Sun X, Ebbesen SD, Chen M. Pressurized Operation of a Planar Solid Oxide Cell Stack. Fuel Cells 2016;16(2):205–18. https://doi.org/10.1002/fuce.201500180.

[102] Posdziech O, Schwarze K, Brabandt J. Efficient hydrogen production for industry and electricity storage via high-temperature electrolysis. Int J Hydrogen Energy 2019;44(35):19089–101. https://doi.org/10.1016/j.ijhydene.2018.05.169.

[103] Mogensen MB, Chen M, Frandsen HL, Graves C, Hansen JB, Hansen KV, et al. Reversible solid-oxide cells for clean and sustainable energy. Clean Energy 2019;3(3):175–201.

[104] Lehtinen T, Noponen M. Solid Oxide Electrolyser Demonstrator Development at Elcogen. ECS Trans 2021;103(1):1939–44. https://doi.org/10.1149/10301.1939ecst.

[105] Wang L, Chen M, Küngas R, Lin T-E, Diethelm S, Maréchal F, et al. Power-to-fuels via solid-oxide electrolyzer: Operating window and techno-economics. Renewable Sustainable Energy Rev 2019;110:174–87.

[106] Hansen JB, Hendriksen PV. The SOC4NH3 Project. Production and Use of Ammonia by Solid Oxide Cells. ECS Trans 2019;91(1):2455–65. https://doi.org/10.1149/09101.2455ecst.